Vision Based Navigation for Autonomous Cooperative Docking of CubeSats

Camille Pirat [a],[*], Finn Ankersen [b], Roger Walker [b], Volker Gass [a]

[a] *Swiss Federal Institute of Technology in Lausanne (EPFL), Station 13, 1015, Lausanne, Switzerland*
[b] *European Space Agency - ESTEC, Keplerlaan 1, 2201AZ, Noordwijk, The Netherlands*

ABSTRACT

A realistic rendezvous and docking navigation solution applicable to CubeSats is investigated. The scalability analysis of the ESA Autonomous Transfer Vehicle Guidance, Navigation & Control (GNC) performances and the Russian docking system, shows that the docking of two CubeSats would require a lateral control performance of the order of 1 cm. Line of sight constraints and multipath effects affecting Global Navigation Satellite System (GNSS) measurements in close proximity prevent the use of this sensor for the final approach. This consideration and the high control accuracy requirement led to the use of vision sensors for the final 10 m of the rendezvous and docking sequence. A single monocular camera on the chaser satellite and various sets of Light-Emitting Diodes (LEDs) on the target vehicle ensure the observability of the system throughout the approach trajectory. The simple and novel formulation of the measurement equations allows differentiating unambiguously rotations from translations between the target and chaser docking port and allows a navigation performance better than 1 mm at docking. Furthermore, the non-linear measurement equations can be solved in order to provide an analytic navigation solution. This solution can be used to monitor the navigation filter solution and ensure its stability, adding an extra layer of robustness for autonomous rendezvous and docking. The navigation filter initialization is addressed in detail. The proposed method is able to differentiate LEDs signals from Sun reflections as demonstrated by experimental data. The navigation filter uses a comprehensive linearised coupled rotation/translation dynamics, describing the chaser to target docking port motion. The handover, between GNSS and vision sensor measurements, is assessed. The performances of the navigation function along the approach trajectory is discussed.

1. Introduction

Rendezvous & Docking (RVD) missions can be separated in three distinct phases. The first part of such a mission, called Phasing, follows the launch and aims at decreasing the in-plane phase angle and altitude difference between the chaser and target satellites. Once the chaser has caught up the target and is trailing behind, typically by a few tens of kilometre below and behind, a first contact between the two satellites can be established and the relative position of the chaser with respect to the target, can be obtained. This phase, called Homing is directly followed by the Closing phase which aims at bringing the chaser to ranges between tens to few hundreds of meters (depending on the mission). The last phase is the final approach, ending with the docking itself, during which a relative state between the docking ports of the target and the chaser is typically required. Achieving the necessary control accuracy for a successful docking between two cooperative spacecraft requires a robust and efficient navigation solution. Early in the space history, navigation

techniques specifically for docking were developed. The Russian (Soviet) Kurs system relies on RF-sensors and provides a navigation solution ranging from a few hundreds of kilometers down to docking and is still used today on the Soyuz and Progress vehicles when rendezvous and docking with the International Space Station (ISS) [1, p.245]. At the same time, the USA were solving the same problem but using Line of Sight (LoS) techniques [2]. Angle only navigation was used first on the Gemini missions and later on for the Apollo programme. Today far range rendezvous metrology systems for relative positioning rely mainly on GNSS. Carrier Phase Differential GPS (CDGPS) can achieve ~10 cm accuracy [3] and supposedly even ~1 mm [4]. However, LoS constraints and multipath effect usually prevent the use of this sensor for the docking of two satellites, as it was the case for a docking with the ISS. For the European Space Agency (ESA) Automated Transfer Vehicle (ATV) mission, an absolute GNSS solution was used for the phasing manoeuvres and then CDGPS down to a range of 250 m from the ISS [5]. The last part of the ATV mission was relying on Vision Based Navigation (VBN) using

---

retroreflectors positioned at various places on the ISS that were illuminated using a laser and observed by a camera [6]. Solving the perspective n-points problem, a 6 Degrees of Freedom (DoF) navigation solution could be obtained. This same system was used for the docking phase during which the state from the target docking port to the chaser port was required. Solving the perspective problem is quite challenging and is still today an active field of research [7,8]. The MIT SPHERES experiments on-board the ISS are using such technique for the relative navigation. A set of four coplanar fiducial markers (passive) are observed by a camera [9]. Once detected, the collinearity equations [10] are iteratively solved and filtered to obtain the 6 DoF relative state estimate. The image processing algorithms involved in detecting the markers usually require heavy computational load. The simplest approach is to use active illumination beacons such as LEDs. [11] proposes a solution for relative navigation using four coplanar visible LEDs and an Infra-Red (IR) one. The four visible LEDs, detected by a monocular camera, are first used to solve the perspective 3-points problem [7]. The solution is then used as a starting point to solve a non-linear problem in which the IR LED, observed by a photo-diode, is used to improve the range determination. To further improve the LEDs detection, [12] and [13] modulate the current fed to the LEDs at a known frequency (typically few kHz). The LEDs are detected using a position sensing diode and by demodulating the signal and solving the perspective problem iteratively, a 6 DoF relative state can be obtained. The PRISMA mission [14] is one of the latest achievement in terms of autonomous relative state estimation using a vision sensor. By using a set of 5 IR LEDs positioned in a non-collinear pattern [15,16]. The 6 DoF estimation was obtained solving the perspective 4-points problem [17].

The solutions mentioned above are appealing as the pattern observed by the camera lays in a plane and can easily be incorporated on a CubeSat. However, the computational load required by the non-linear solvers is important, especially if the obtained solution needs to be further filtered as any vision sensor produces a noisy signal. Extended Kalman filters (EKFs) are usually selected as they use the dynamics of the system to improve the solution and are easily tunable. As an EKF will most probably have to be used in any case, a solution which would require less computational load than the perspective n-points problem was sought for the problem addressed in the paper.

Another approach for determining the 6 DoF relative state between two spacecraft was proposed by Ref. [18] and was used by NASA [16]. Four beacons positioned in a cross pattern with a fifth out-of-plane beacon laying in the centre of the cross, is used. The position is determined by solving non-linear equations, formed by the observation vectors between the ith beacon and the camera CCD, using a Newton-Raphson method. The obtained vector are then used in a TRIAD or QUEST algorithm [19] to get the relative attitude. The ATV rendezvous monitoring system offers an elegant solution to the relative state determination problem. A monocular camera on the ISS was filming a circular pattern attached to the ATV. An internal cross was laying on a different plane and could then provide a visual indication of the ATV relative attitude and position [1,20]. An analytical solution for the LoS and attitude angles determination was obtained. However, this solution relies on the assumption that during a RVD mission, relative attitude and LoS angles are small and are thus all decoupled from each other, which may not be the case if the LEDs and the camera sensor are not aligned because of system constraints.

The VBN solution proposed in this paper will use the same cross-shaped LED pattern, with one out-of-plane, as in Ref. [18]. The novel non-linear measurement equations can directly be used in an EKF without needing to use first a non-linear solver and a TRIAD or QUEST algorithm. Furthermore, the non-linear equations can be solved analytically to obtain a deterministic solution. Contrary to the ATV monitoring algorithm, which provides an analytical solution for small relative LoS and attitude angles, the proposed solution works for any relative rotation/position. An important aspect for the docking of two satellites is that a rotation of the target satellite translates into a rotation and a translation

for the chaser satellite. The sought formulation of the 6 DoF relative state determination allows to differentiate unambiguously rotations from translations and provides the chaser the shortest path to follow to align itself with the target docking port. As a result, the chaser translation and rotation can be performed at the same time in an optimal way. The first detection of the LEDs for the navigation filter initialization will be performed using the geometrical characteristics of the patterns. The algorithm is able to detect the LEDs even if the Sun or the Earth are in the Field of View (FoV) and can efficiently reject reflections on the CubeSat surface.

This paper will start with a brief description of a RVD scenario that is applicable to CubeSats and a scalability analysis of the ATV and Soyuz/ Progress requirements for the GNC, in section 2. In section 3, the vision navigation solution will be described. Measurement equations and a 6 DoF relative dynamics describing the rotation/translation coupling between the chaser and target docking port will be provided and used in an EKF. A solution for the initialization of the navigation filter and detection of the LEDs by the camera will be discussed. Finally, in section 4, the initialization and performances of the VBN filter will be analysed.

2. Rendezvous scenario and docking requirements

Fig. 1 shows the last part of the rendezvous profile from the end of Closing (point $S2_4$) until docking. The scenario is shown in the LVLH (orbital) frame. The centre of the frame is located at the target centre of mass and its axis are as follow: $\hat{z} = -\frac{r}{r}$, where r is the Target inertial position, and is referred as $\overline{R}$. $\hat{y} = -\frac{r \times v}{|r \times v|}$, where v is the inertial velocity of the Target, and is called $\overline{H}$. Finally $\hat{x}$ completes the direct frame and is referred as $\overline{V}$. The Phasing, Homing and Closing parts will not be discussed here as the strategy used for bringing the chaser satellite down to a 15 m range from the target is assumed to be similar than in Ref. [21].

At $S2_4$, the chaser body frame is aligned with the LVLH frame. It's position is obtained using CDGPS and its attitude is relying on a star tracker, 6 sun sensors, a magnetometer and a 3-axis gyroscope. The fly-around trajectory will align the chaser with the target docking port. At point $S3$, the first handover between CDGPS navigation and Vision Based Navigation takes place. Due to the small spacecraft size, GNSS multipath effects are assumed to be negligible up to this point. The chaser will then move in forced straight line with hold points at 5 m and 2.5 m ranges. Although CDGPS could probably provide an accurate navigation down to a closer range, it was still decided to perform the handover at a 10 m, allowing a sufficient overlap between the two sensors range of use. Indeed, CDGPS performance for CubeSats was not yet properly assessed and a handover at 10 m does not complicate much the VBN design, as it will be shown in section 3.3.

Very few preliminary designs of docking ports exist for CubeSats. The AAREST mission is planning to use a magnetic docking port [22]. The main advantage of such design is that the required accuracy for the docking is only ∼ 30 cm. However, it was deemed not desireable to have a strong magnetic field on-board a CubeSat. Even if the primary attitude
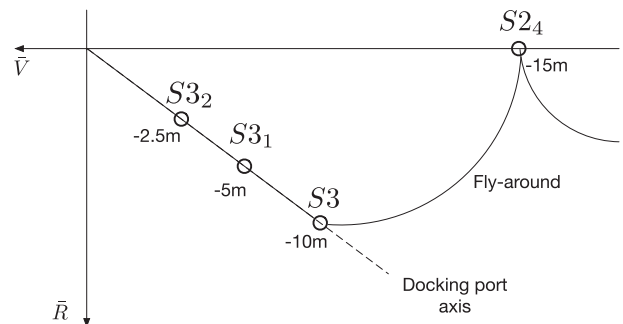

Fig. 1. Docking port-axis acquisition and forced motion until docking (docking port not aligned with LVLH frame).

sensor is the star tracker, the magnetometer is often kept in the navigation function as a backup and could be disturbed the docking mechanism magnetic field. Furthermore, the coupling of this field with the Earth's own field will induce disturbances that the GNC will need to compensate. In Ref. [23], an androgynous mechanism is proposed and can manage 5 deg and 1.5 cm misalignment. It was however never tested in space. The most advanced docking system is probably the MIT Universal Docking Port (UDP) [24]. The control accuracy required is ∼ 1 cm and it can tolerate attitude misalignment of ∼ 2 deg. However, the MIT UDP is used inside the ISS, in a very controlled environment. To gain more insight on the kind of performances that are required for a full RVD mission, a scalability analysis of the ATV performances was done. The ATV is using the Russian "drogue-and-cone" docking system [25]. The cone has a diameter of 800 mm. The docking mechanism tolerates up to 10 cm of lateral misalignment and at most 5 deg. [5]. To be interesting for CubeSats, a docking mechanism shall fit within one CubeSat unit, i.e. $10 \times 10 \times 10$ cm^3. Scaling down linearly the Russian docking system to a CubeSat level leads to a lateral misalignment of ∼ 1.2 cm which is consistent with the MIT UDP performances. It will then be assumed that to have a successful docking, the lateral misalignment shall be better than 1.2 cm and attitude misalignment < 2deg around each axis.

3. Cooperative vision based navigation

3.1. Notation and reference frame

The following mathematical models will be using several reference frames which are described here after.

- The Earth-centred Inertial (ECI) frame is using the J2000 definition and is named I.
- The LVLH frame (or orbital frame) was defined in the previous section and is named o.

To define properly the dynamics of the CubeSat, several frames are needed, as shown on Fig. 2.

- The geometrical frame is physically connected to the CubeSat structure and is fixed with it. It's origin is typically connected to a corner of the CubeSat. It is named g.
- The body frame is located in the geometrical frame. It's origin is at the CubeSat centre of Mass (CoM) and is aligned with the satellite principal axis of inertia. It is named b.
- The docking port frame is located in the geometrical frame. It's location is defined by a translation and a rotation and it is named d.
- The frame used for the Vision Based Navigation is defined like the docking frame and is named n.

Because of fuel depletion, the body frame will move inside the geometrical frame. This variation can be directly treated in the dynamics equations. However, the CoM movement in the geometrical frame cannot be precisely measured on-orbit. Thus, this effect will be treated as an external disturbance and the body frame will be assumed fixed in the geometrical frame. Consequently, the docking frame and VBN frame can
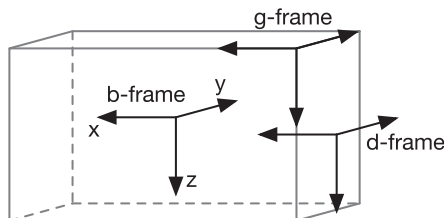
be unambiguously defined with respect to the body frame.

The body frame b, docking port frame d and VBN frame n can be named after the chaser or target satellite, as shown in Fig. 3. $r_{b_t}^{d_t}$ is the position of the target docking port expressed in the target body frame b_t. For rotations, the following notation will be used: $r_{d_t}^{d_t} = A_{d_t b_t} r_{b_t}^{d_t}$, where $A_{d_t b_t}$ maps the frame b_t into the frame d_t. The transpose of $A_{d_t b_t}$ is $A_{d_t b_t}^{\mathrm{T}} = A_{b_t d_t}$.

3.2. Relative dynamics

In this section, the non-linear dynamics for a coupled rotation/translation systems will be derived and linearised. A linearised coupled dynamics can be found in Ref. [26]. It was developed for the docking between the ATV and ISS. Because of the optimal alignment and stability of the ISS in the orbital frame, its motion was approximated by an harmonic oscillator. This assumption could not be done for CubeSats as their attitude is unlikely to be as stable as the ISS one.

3.2.1. Coupled attitude

The attitude dynamics will first be derived and linearised in the orbital frame. The angular rate of a body b with respect to the orbital frame o can be expressed as a function of the body rotation with respect to the inertial frame:

$$\boldsymbol{\omega}_b^{bo} = \boldsymbol{\omega}_b^{bI} - A_{bo} \, \boldsymbol{\omega}_o^{oI} \tag{1}$$

where $\boldsymbol{\omega}_o^{oI}$ is the orbital frame rotation rate with respect to the inertial frame, expressed in the orbital frame, $\boldsymbol{\omega}_o^{oI} = [0 \ -\omega_o \ 0]^{\mathrm{T}}$, with ω_o the orbital mean motion. The usual body dynamics expressed in the inertial frame [27, p.84] is:

$$\dot{\boldsymbol{\omega}}_b^{bI} = I_b^{-1} \left[\boldsymbol{T}_b - \boldsymbol{\omega}_b^{bI} \times \left(I_b \, \boldsymbol{\omega}_b^{bI} \right) \right] \tag{2}$$

where I_b is the inertia tensor of the rigid body. The body dynamics with respect to the orbital frame can be obtained using (1) into (2):

$$\dot{\boldsymbol{\omega}}_b^{bo} = I_b^{-1} \left[\boldsymbol{T}_b - \left(\boldsymbol{\omega}_b^{bo} + A_{bo} \, \boldsymbol{\omega}_o^{oI} \right) \times \left(I_b \left(\boldsymbol{\omega}_b^{bo} + A_{bo} \, \boldsymbol{\omega}_o^{oI} \right) \right) \right] \tag{3}$$

where $\boldsymbol{T}_b$ is the control torque in the body frame.

The kinematics is obtained considering the 1-2-3 Euler sequence [27, p.363]. The 3-2-1 sequence is usually preferred but is not convenient for the metrology system that will be presented in the next section. The notation $\boldsymbol{\alpha} \equiv [\alpha \ \beta \ \gamma]^{\mathrm{T}}$ will be used such that $R_{123}(\boldsymbol{\alpha}) = R_3(\gamma)R_2(\beta)R_1(\alpha)$, where $R_i, i = 1, 2, 3$, are the usual rotation matrices for direct reference frames.

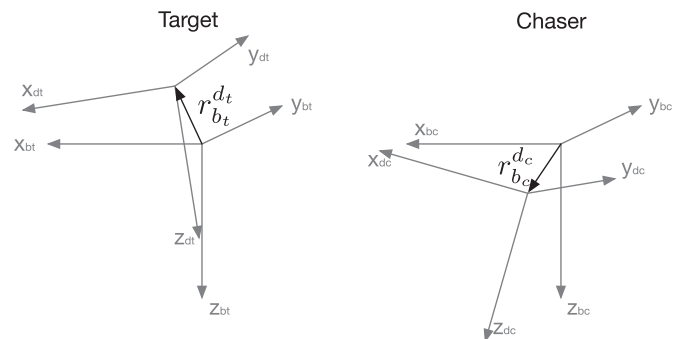$$\dot{\boldsymbol{\alpha}} = B_{123}(\beta, \gamma) \boldsymbol{\omega}_b^{bo} \tag{4}$$

with

Fig. 3. Body frame and docking port frame for the target and chaser satellites. The exact same convention is used for the navigation frame n.

Fig. 2. Body frame, docking port frame and geometrical frame.

$$B_{123}(\beta,\gamma) = \begin{bmatrix} \sec\beta\cos\gamma & -\sec\beta\sin\gamma & 0 \\ \sin\gamma & \cos\gamma & 0 \\ -\tan\beta\cos\gamma & \tan\beta\sin\gamma & 1 \end{bmatrix} \tag{5}$$

The system can be written in one non-linear function

$$\begin{bmatrix} \dot{\boldsymbol{\alpha}} \\ \dot{\boldsymbol{\omega}}_b^{bo} \end{bmatrix} = \boldsymbol{f}(\boldsymbol{\alpha}, \boldsymbol{\omega}_b^{bo}, \boldsymbol{T}_b) \tag{6}$$

and can be linearised around given points $\overline{\boldsymbol{\alpha}}, \overline{\boldsymbol{\omega}}_b^{bo}, \overline{\boldsymbol{T}}_b$:

$$\begin{aligned} \boldsymbol{f}(\boldsymbol{\alpha}, \boldsymbol{\omega}_b^{bo}, \boldsymbol{T}_b) &\approx \boldsymbol{f}(\overline{\boldsymbol{\alpha}}, \overline{\boldsymbol{\omega}}_b^{bo}, \overline{\boldsymbol{T}}_b) + \frac{\partial \boldsymbol{f}}{\partial \boldsymbol{\alpha}}\Big|_{\overline{\boldsymbol{\alpha}}, \overline{\boldsymbol{\omega}}_b^{bo}, \overline{\boldsymbol{T}}_b} (\boldsymbol{\alpha} - \overline{\boldsymbol{\alpha}}) \\ &+ \frac{\partial \boldsymbol{f}}{\partial \boldsymbol{\omega}_b^{bo}}\Big|_{\overline{\boldsymbol{\alpha}}, \overline{\boldsymbol{\omega}}_b^{bo}, \overline{\boldsymbol{T}}_b} (\boldsymbol{\omega}_b^{bo} - \overline{\boldsymbol{\omega}}_b^{bo}) + \frac{\partial \boldsymbol{f}}{\partial \boldsymbol{T}_b}\Big|_{\overline{\boldsymbol{\alpha}}, \overline{\boldsymbol{\omega}}_b^{bo}, \overline{\boldsymbol{T}}_b} (\boldsymbol{T}_b - \overline{\boldsymbol{T}}_b) \end{aligned} \tag{7}$$

Let's first consider the simple case where the satellite is aligned with the orbital frame, i.e. $\overline{\boldsymbol{\alpha}} = \overline{\boldsymbol{\omega}}_b^{bo} = \overline{\boldsymbol{T}}_b = 0$. In this case, considering $\boldsymbol{x} = [\boldsymbol{\alpha}\ \boldsymbol{\omega}_b^{bo}]^{\mathrm{T}}$, and assuming a diagonal inertia tensor, the state-space equation is:

$$\dot{\boldsymbol{x}} = \begin{bmatrix} 0 & A_{12} \\ A_{21} & A_{22} \end{bmatrix} \boldsymbol{x} + \begin{bmatrix} 0 \\ B_{21} \end{bmatrix} \boldsymbol{T}_b \tag{8}$$

with A_{12} the 3×3 identity matrix,

$$A_{21} = \begin{bmatrix} \omega_o^2 \dfrac{I_{33} - I_{22}}{I_{11}} & 0 & 0 \\ 0 & 0 & 0 \\ 0 & 0 & \omega_o^2 \dfrac{I_{22} - I_{11}}{I_{33}} \end{bmatrix} \tag{9}$$

$$A_{22} = \begin{bmatrix} 0 & 0 & \omega_o \dfrac{I_{33} - I_{22}}{I_{11}} \\ 0 & 0 & 0 \\ \omega_o \dfrac{I_{22} - I_{11}}{I_{33}} & 0 & 0 \end{bmatrix} \tag{10}$$

$$B_{21} = \begin{bmatrix} \dfrac{1}{I_{11}} & 0 & 0 \\ 0 & \dfrac{1}{I_{22}} & 0 \\ 0 & 0 & \dfrac{1}{I_{33}} \end{bmatrix} \tag{11}$$

It is important to note that if the satellite body frame is not aligned with the orbital frame, i.e. the linearisation point $\overline{\boldsymbol{\alpha}} \neq 0$, then $A_{12} = B_{123}(\overline{\beta}, \overline{\gamma})$, where $B_{123}(\overline{\beta}, \overline{\gamma})$ is given by (5). In this case, if $\beta = \pm\pi/2$, then A_{12} diverges. This divergence for certain angles is a well known property of the Euler angles and is often referred to as "gimbal-lock". Still for $\overline{\boldsymbol{\alpha}} \neq 0$, A_{21} and A_{22} become a function of the inertia tensor expressed in the rotated frame. Further more as $\overline{\boldsymbol{\alpha}} \neq 0$ is not an equilibrium point of the non-linear dynamics, two constant terms are added to the linearisation:

1. $\boldsymbol{f}(\overline{\boldsymbol{\alpha}}, \overline{\boldsymbol{\omega}}_b^{bo}, \overline{\boldsymbol{T}}_b)$
2. $-\partial \boldsymbol{f}/\partial \boldsymbol{\alpha}\big|_{\overline{\boldsymbol{\alpha}}, \overline{\boldsymbol{\omega}}_b^{bo}, \overline{\boldsymbol{T}}_b} \overline{\boldsymbol{\alpha}}$

These reflect the fact that a constant rotation with no external torques can only take place around a principal axis of inertia. For non trivial rigid body, a constant force needs to be applied to maintain a given rotation rate. Otherwise, the dynamics will converge toward a new orientation (i.e. vectorial basis) which makes the inertia tensor diagonal, or in other word, its eigenstate. This fact impacts the state-space formulation and

these constant terms can be either treated as feed-forward terms or the controller that will be used to control the system will need to add a constant correction.

The aim is to derive a docking port to docking port dynamics. The attitude dynamics (3) needs then to be expressed in a frame d as shown in Fig. 3. As the rotation matrix mapping frame b to frame d is constant, no extra derivative term will appear. However, the inertia tensor I_b needs to be expressed in the new frame d, taking into account the rotation and the translation. Thus, for a frame d, with orientation A_{db} and position $\boldsymbol{r}_b^d$, using the parallel axis theorem [27, p.81], the inertia is given by

$$I_d = A_{db}(I_b + m[||\boldsymbol{r}_b^d||^2 I_3 - \boldsymbol{r}_b^d \boldsymbol{r}_b^{d\mathrm{T}}])A_{db}^{\mathrm{T}} \tag{12}$$

It should be noted that I_d will not be diagonal any more as it is now expressed in an arbitrary rotated frame. For the sake of clarity, the equations provided in this paper will assume a diagonal inertia tensor. However, the simulation will use the complete formulation with a non-diagonal tensor.

The attitude dynamics expressed in an arbitrary frame d, using (3), is

$$\dot{\boldsymbol{\omega}}_d^{do} = I_d^{-1}\big[\boldsymbol{T}_d - (\boldsymbol{\omega}_d^{do} + A_{do}\boldsymbol{\omega}_o^{oI}) \times (I_d(\boldsymbol{\omega}_d^{do} + A_{do}\boldsymbol{\omega}_o^{oI}))\big] \tag{13}$$

with $A_{do} = A_{db}A_{bo}$. The kinematics equations are the same as (4).

The relative dynamics $\dot{\boldsymbol{\omega}}_{d_c}^{d_c d_t}$, i.e. the rotation of the chaser docking frame d_c with respect to d_t expressed in d_c, can be derived. Starting from the angular velocities composition and using the attitude matrix $A_{d_c d_t}$, mapping frame d_t into frame d_c, the relative angular velocity is

$$\boldsymbol{\omega}_{d_c}^{d_c d_t} = \boldsymbol{\omega}_{d_c}^{d_c o} - A_{d_c d_t}\boldsymbol{\omega}_{d_t}^{d_t o} \tag{14}$$

in which $\boldsymbol{\omega}_{d_c}^{d_c o}$ and $\boldsymbol{\omega}_{d_t}^{d_t o}$ are given by (13). Differentiating with respect to time leads to the sought equation:

$$\dot{\boldsymbol{\omega}}_{d_c}^{d_c d_t} = \dot{\boldsymbol{\omega}}_{d_c}^{d_c o} - A_{d_c d_t}\dot{\boldsymbol{\omega}}_{d_t}^{d_t o} + \boldsymbol{\omega}_{d_c}^{d_c d_t} \times (A_{d_c d_t}\boldsymbol{\omega}_{d_t}^{d_t o}) \tag{15}$$

$\dot{\boldsymbol{\omega}}_{d_c}^{d_c o}$ is given by:

$$\dot{\boldsymbol{\omega}}_{d_c}^{d_c o} = I_{d_c}^{-1}\big[\boldsymbol{T}_{d_c} - (\boldsymbol{\omega}_{d_c}^{d_c o} + A_{d_c o}\boldsymbol{\omega}_o^{oI}) \times (I_{d_c}(\boldsymbol{\omega}_{d_c}^{d_c o} + A_{d_c o}\boldsymbol{\omega}_o^{oI}))\big] \tag{16}$$

As $A_{d_c o} = A_{d_c d_t}A_{d_t o}$ and $\boldsymbol{\omega}_{d_c}^{d_c o} = \boldsymbol{\omega}_{d_c}^{d_c d_t} + A_{d_c d_t}\boldsymbol{\omega}_{d_t}^{d_t o}$, (15) can be expressed as a function of the relative attitude variables and of the target attitude. The kinematics for the relative attitude is given by (4):

$$\begin{aligned} \dot{\boldsymbol{\alpha}}^{d_c d_t} &= B_{123}(\beta^{d_c d_t}, \gamma^{d_c d_t})\ \boldsymbol{\omega}_{d_c}^{d_c d_t} \\ \dot{\boldsymbol{\alpha}}^{d_t o} &= B_{123}(\beta^{d_t o}, \gamma^{d_t o})\ \boldsymbol{\omega}_{d_t}^{d_t o} \end{aligned} \tag{17}$$

A state-space model can be obtained by linearising the non-linear dynamics (13) and (15), and kinematics (17). The state vector will be defined as $\boldsymbol{x} = [\boldsymbol{\alpha}^{d_c d_t}, \boldsymbol{\omega}_{d_c}^{d_c d_t}, \boldsymbol{\alpha}^{d_t o}, \boldsymbol{\omega}_{d_t}^{d_t o}]^{\mathrm{T}}$ and the control input $\boldsymbol{u} = [\boldsymbol{T}_{d_c}, \boldsymbol{T}_{d_t}]^{\mathrm{T}}$. $\boldsymbol{\alpha}^{d_c d_t}$ is a vector containing the three Euler angles for the relative attitude matrix $A_{d_c d_t}$, and $\boldsymbol{T}_{d_c}$ and $\boldsymbol{T}_{d_t}$ are the chaser and target control torques. As before, the 1-2-3 Euler sequence is preferred, although this is valid for any Euler sequence. The linearisation points will be chosen as follow:

- The target docking frame d_t can have any orientation in the orbital frame but is not rotating: $\overline{\boldsymbol{\alpha}}^{d_t o} =$ const. and $\overline{\boldsymbol{\omega}}_{d_t}^{d_t o} = 0$
- The chaser is aligned with the target and is not rotating: $\overline{\boldsymbol{\alpha}}^{d_c d_t} = \overline{\boldsymbol{\omega}}_{d_c}^{d_c d_t} = 0$

Writing the state-space as

$$\dot{\boldsymbol{x}} = A\boldsymbol{x} + B\boldsymbol{u} \tag{18}$$

the matrices A and B are given by:

$$A = \begin{bmatrix} 0 & A_{12} & 0 & 0 \\ A_{21} & A_{22} & A_{23} & A_{24} \\ 0 & 0 & 0 & A_{34} \\ 0 & 0 & A_{43} & A_{44} \end{bmatrix} \tag{19}$$

$$B = \begin{bmatrix} 0 & 0 \\ B_{21} & B_{22} \\ 0 & 0 \\ 0 & B_{42} \end{bmatrix} \tag{20}$$

A and B will not be explicitly shown for the general case as the analytical expressions are complex. The case in which the target satellite is aligned with the orbital frame already allows to picture the impact of the coupling.

As in (8), A_{12} and A_{34} are 3×3 identity matrices. The other elements are:

$$A_{21} = \begin{pmatrix} -\dfrac{\omega_o^2 \left(I_{d_t,22} - I_{d_t,33}\right)}{I_{d_c,11}} & 0 & 0 \\ 0 & 0 & 0 \\ 0 & 0 & \dfrac{\omega_o^2 \left(I_{d_t,11} - I_{d_t,22}\right)}{I_{d_c,33}} \end{pmatrix} \tag{21}$$

$$A_{22} = \begin{pmatrix} 0 & 0 & -\dfrac{\omega_o \left(I_{d_t,22} - I_{d_t,33}\right)}{I_{d_c,11}} \\ 0 & 0 & 0 \\ -\dfrac{\omega_o \left(I_{d_t,11} - I_{d_t,22}\right)}{I_{d_c,33}} & 0 & 0 \end{pmatrix} \tag{22}$$

$$A_{23} = \begin{pmatrix} \dfrac{\omega_o^2 \left(I_{d_c,11} - I_{d_t,11}\right)\left(I_{d_t,22} - I_{d_t,33}\right)}{I_{d_c,11} I_{d_t,11}} & 0 & 0 \\ 0 & 0 & 0 \\ 0 & 0 & -\dfrac{\omega_o^2 \left(I_{d_c,33} - I_{d_t,33}\right)\left(I_{d_t,11} - I_{d_t,22}\right)}{I_{d_c,33} I_{d_t,33}} \end{pmatrix} \tag{23}$$

$$A_{24} = \begin{pmatrix} 0 & 0 & \dfrac{\omega_o \left(I_{d_c,11} - I_{d_t,11}\right)\left(I_{d_t,22} - I_{d_t,33}\right)}{I_{d_c,11} I_{d_t,11}} \\ 0 & 0 & 0 \\ \dfrac{\omega_o \left(I_{d_c,33} - I_{d_t,33}\right)\left(I_{d_t,11} - I_{d_t,22}\right)}{I_{d_c,33} I_{d_t,33}} & 0 & 0 \end{pmatrix} \tag{24}$$

which are reflecting the attitude coupling of the chaser with the target. The elements A_{43} and A_{44} are strictly identical to (8) as the target is not coupled to the chaser. The coupling appears also explicitly in the control input matrix B. B_{21} and B_{41} have the usual form as in (11), i.e. $B_{21} = I_{d_c}^{-1}$ and $B_{42} = I_{d_t}^{-1}$. The coupling term $B_{22} = -B_{42}$ reflects perfectly the fact that a positive rotation of the target translates into a negative rotation for the chaser. Finally, it should be noted that the in the case of $\overline{\alpha}^{d_t o} \neq 0$, constant terms will appear as it was previously mentioned.

3.2.2. Coupled position

In this section the state-space model for the relative position will be derived. Combining it with the relative attitude state-space will lead to a complete formulation of the 6 DoF translation/rotation coupled system.

The CoM to CoM position between the chaser and target is given by $s_I^{ct} = r_I^c - r_I^t$. Expressing it in the orbital frame, differentiating two times and linearising around the target position would lead to the Hill's equations [28]. The port to port relative distance expressed in the target docking port frame is (see Fig. 4):
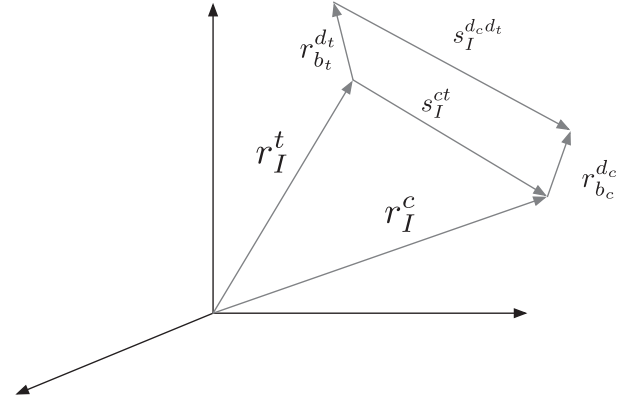

Fig. 4. Relative position of the chaser with respect to the target in Inertial frame and docking port to docking port relative position [26].

$$\boldsymbol{s}_{d_t}^{d_c d_t} = A_{d_t o} A_{oI} \boldsymbol{s}_I^{ct} + \underbrace{A_{d_t d_c} A_{d_c b_c} \boldsymbol{r}_{b_c}^{d_c}}_{=\boldsymbol{r}_{d_c}^{d_c}} - \underbrace{A_{d_t b_t} \boldsymbol{r}_{b_t}^{d_t}}_{=\boldsymbol{r}_{d_t}^{d_t}} \tag{25}$$

$A_{d_t d_c}$ is given by the relative attitude kinematics and $A_{d_t o}$ by the target attitude kinematics. Differentiating (25) leads to the velocity:

$$\begin{aligned} \dot{\boldsymbol{s}}_{d_t}^{d_c d_t} &= -\boldsymbol{\omega}_{d_t}^{d_t o} \times A_{d_t o} A_{oI} \boldsymbol{s}_I^{ct} - A_{d_t o} \left(\boldsymbol{\omega}_o^{oI} \times A_{oI} \boldsymbol{s}_I^{ct}\right) \\ &\quad + A_{d_t o} A_{oI} \dot{\boldsymbol{s}}_I^{ct} - \boldsymbol{\omega}_{d_t}^{d_t d_c} \times A_{d_t d_c} \boldsymbol{r}_{d_c}^{d_c} \end{aligned} \tag{26}$$

The acceleration can finally be obtained differentiating (26):

$$\begin{aligned} \ddot{\boldsymbol{s}}_{d_t}^{d_c d_t} &= -\dot{\boldsymbol{\omega}}_{d_t}^{d_t o} \times \boldsymbol{s}_{d_t}^{ct} - \boldsymbol{\omega}_{d_t}^{d_t o} \times \boldsymbol{\omega}_{d_t}^{d_t o} \times \boldsymbol{s}_{d_t}^{ct} - 2\boldsymbol{\omega}_{d_t}^{d_t o} \times \dot{\boldsymbol{s}}_{d_t}^{d_c d_t} - \left(A_{d_t o}\boldsymbol{\omega}_o^{oI}\right) \\ &\quad \times \left(A_{d_t o}\boldsymbol{\omega}_o^{oI}\right) \times \boldsymbol{s}_{d_t}^{ct} - 2\left(A_{d_t o}\boldsymbol{\omega}_o^{oI}\right) \times \dot{\boldsymbol{s}}_{d_t}^{d_c d_t} - 2\left(A_{d_t o}\boldsymbol{\omega}_o^{oI}\right) \times \boldsymbol{\omega}_{d_t}^{d_t o} \times \boldsymbol{s}_{d_t}^{ct} \\ &\quad + 2\left(A_{d_t o}\boldsymbol{\omega}_o^{oI} + \boldsymbol{\omega}_{d_t}^{d_t o}\right) \times \left(A_{d_c d_t}^{\mathrm{T}}\boldsymbol{\omega}_{d_c}^{d_c d_t}\right) \times \left(A_{d_c d_t}^{\mathrm{T}}\boldsymbol{r}_{d_c}^{d_c}\right) + \left(A_{d_c d_t}^{\mathrm{T}}\dot{\boldsymbol{\omega}}_{d_c}^{d_c d_t}\right) \\ &\quad \times \left(A_{d_c d_t}^{\mathrm{T}}\boldsymbol{r}_{d_c}^{d_c}\right) + 2\left(A_{d_c d_t}^{\mathrm{T}}\boldsymbol{\omega}_{d_c}^{d_c d_t}\right) \times \left(A_{d_c d_t}^{\mathrm{T}}\boldsymbol{\omega}_{d_c}^{d_c d_t}\right) \times \left(A_{d_c d_t}^{\mathrm{T}}\boldsymbol{r}_{d_c}^{d_c}\right) + \boldsymbol{F}_{d_t}^{ct} \end{aligned} \tag{27}$$

where

$$\boldsymbol{s}_{d_t}^{ct} = A_{d_t o} \boldsymbol{r}_o^t + \boldsymbol{s}_{d_t}^{d_c d_t} - A_{d_c d_t}^{\mathrm{T}} \boldsymbol{r}_{d_c}^{d_c} + \boldsymbol{r}_{d_t}^{d_t} \tag{28}$$

(27) should look familiar as it represents nothing more than the equations of motion of a solid body in a non-inertial frame. The Coriolis and centripetal inertial forces due to the docking frame d_t and orbital frame o rotations can clearly be identified. Extra Coriolis/centripetal-like terms resulting from the coupling between the frames are also present. $\boldsymbol{F}_{d_t}^{ct}$ contains the usual gravitational terms and control input forces:

$$\begin{aligned} \boldsymbol{F}_{d_t}^{ct} &= \mu \frac{A_{d_t o}\boldsymbol{r}_o^t}{\|\boldsymbol{r}_o^t\|^3} - \mu \frac{A_{d_t o}\boldsymbol{r}_o^t + \boldsymbol{s}_{d_t}^{d_c d_t} - A_{d_c d_t}^{\mathrm{T}}\boldsymbol{r}_{d_c}^{d_c} + \boldsymbol{r}_{d_t}^{d_t}}{\left\|A_{d_t o}\boldsymbol{r}_o^t + \boldsymbol{s}_{d_t}^{d_c d_t} - A_{d_c d_t}^{\mathrm{T}}\boldsymbol{r}_{d_c}^{d_c} + \boldsymbol{r}_{d_t}^{d_t}\right\|^3} \\ &\quad + A_{d_c d_t}^{\mathrm{T}} \frac{\boldsymbol{F}_{d_c}}{m_c} \end{aligned} \tag{29}$$

$\boldsymbol{F}_{d_c}$ is the control force provided by the chaser in the chaser docking frame and m_c is the chaser mass. $\boldsymbol{r}_o^t$ is the target position expressed in the orbital frame: $\boldsymbol{r}_o^t = [0\ 0\ -r_o^t]^{\mathrm{T}}$. (29) is obtained from the usual acceleration term in the Newton equations:

$$\boldsymbol{a}_I^{ct} = \mu \frac{\boldsymbol{r}_I^t}{\|\boldsymbol{r}_I^t\|^3} - \mu \frac{\boldsymbol{r}_I^t + \boldsymbol{s}_I^{ct}}{\|\boldsymbol{r}_I^t + \boldsymbol{s}_I^{ct}\|^3} + \frac{\boldsymbol{F}_I}{m_c} \tag{30}$$

which is then expressed in the docking port frame d_t and rearranged using (28).

(27) was arranged in a way such that only the target attitude dynamics in the orbital frame appears as well as the port to port relative

attitude dynamics. This will be of a certain advantage when writing the state-space model as the plant output $\boldsymbol{y}$ will be exactly equal to the state $\boldsymbol{x}$. The output equation of a linearised plant is of the form $\boldsymbol{y} = C\boldsymbol{x} + D\boldsymbol{u}$. In the proposed formulation C is equal to the identity and $D = 0$ and can thus be conveniently used in a full-state feedback formulation.

Defining the state vector as

$$\boldsymbol{x} = \left[\boldsymbol{\alpha}^{d_c d_t}, \boldsymbol{\omega}^{d_c d_t}_{d_c}, \boldsymbol{\alpha}^{d_t o}, \boldsymbol{\omega}^{d_t o}_{d_t}, \boldsymbol{s}^{d_c d_t}_{d_t}, \dot{\boldsymbol{s}}^{d_c d_t}_{d_t}\right]^{\mathrm{T}}$$

and the control input

$$\boldsymbol{u} = \left[\boldsymbol{T}_{d_c}, \boldsymbol{T}_{d_t}, \boldsymbol{F}_{d_c}\right]^{\mathrm{T}}$$

(27) together with the relative attitude dynamics (13), (15) and kinematics (17) can be linearised around the following points:

- $\overline{\boldsymbol{\alpha}}^{d_t o} = const.$ and $\overline{\boldsymbol{\omega}}^{d_t o}_{d_t} = 0$
- $\overline{\boldsymbol{\alpha}}^{d_c d_t} = \overline{\boldsymbol{\omega}}^{d_c d_t}_{d_c} = 0$
- $\boldsymbol{s}^{d_c d_t}_{d_t} = \dot{\boldsymbol{s}}^{d_c d_t}_{d_t} = 0$
- $\boldsymbol{T}_{d_c} = \boldsymbol{T}_{d_t} = \boldsymbol{F}_{d_c} = 0$

The state-space model for the 6 DoF port to port dynamics is:

$$\begin{aligned}\dot{\boldsymbol{x}} &= A\boldsymbol{x} + B\boldsymbol{u} \\ \boldsymbol{y} &= C\boldsymbol{x} + D\boldsymbol{u}\end{aligned} \tag{31}$$

with[1]

$$A = \begin{bmatrix} 0 & A_{12} & 0 & 0 & 0 & 0 \\ A_{21} & A_{22} & A_{23} & A_{24} & 0 & 0 \\ 0 & 0 & 0 & A_{34} & 0 & 0 \\ 0 & 0 & A_{43} & A_{44} & 0 & 0 \\ 0 & 0 & 0 & 0 & 0 & A_{56} \\ A_{61} & A_{62} & A_{63} & A_{64} & A_{65} & A_{66} \end{bmatrix} \tag{32}$$

$$B = \begin{bmatrix} 0 & 0 & 0 \\ B_{21} & B_{22} & 0 \\ 0 & 0 & 0 \\ 0 & B_{42} & 0 \\ 0 & 0 & 0 \\ B_{61} & B_{62} & B_{63} \end{bmatrix} \tag{33}$$

Finally, in (31), the matrix C is the identity and $D = 0$. In (32), matrix blocks corresponding to the relative attitude were already described in (19). The terms A_{61} to A_{66} are long expressions in which the chaser and target inertia appear as well as the docking ports position $\boldsymbol{r}^{d_c}_{d_c}$ and $\boldsymbol{r}^{d_t}_{d_t}$. A_{62} is given as an example for the case in which the target is aligned with the orbital frame:

$$A_{62} = \begin{bmatrix} -\dfrac{r^{d_c}_{d_c,y}\omega_o\left(2I_{d_c,33} - I_{d_t,11} + I_{d_t,22}\right)}{I_{d_c,33}} & 2r^{d_c}_{d_c,x}\omega_o & 0 \\[2ex] -\dfrac{r^{d_c}_{d_c,x}\omega_o\left(I_{d_t,11} - I_{d_t,22}\right)}{I_{d_c,33}} & 0 & \dfrac{r^{d_c}_{d_c,z}\omega_o\left(I_{d_t,22} - I_{d_t,33}\right)}{I_{d_c,11}} \\[2ex] 0 & 2r^{d_c}_{d_c,z}\omega_o & -\dfrac{r^{d_c}_{d_c,y}\omega_o\left(2I_{d_c,11} + I_{d_t,22} - I_{d_t,33}\right)}{I_{d_c,11}} \end{bmatrix} \tag{34}$$

It describes the effect of the relative rotation rate on the relative position. A_{56} is the 3×3 identity matrix. In the simple case where the target and chaser are aligned and fixed with the orbital frame and that $\boldsymbol{r}^{d_t}_{d_t} = \boldsymbol{r}^{d_c}_{d_c} = 0$, then A_{61} to A_{64} are null and A_{65}, A_{66} transform into the well known Hill's equations [28].

Finally for the input matrix B in (33), B_{21}, B_{22} and B_{24} are the same as

for the relative attitude state-space model (19). B_{61}, representing the effect of the chaser rotation on the position is:

$$B_{61} = \begin{bmatrix} 0 & \dfrac{r^{d_c}_{d_c,z}}{I_{d_c,22}} & -\dfrac{r^{d_c}_{d_c,y}}{I_{d_c,33}} \\[2ex] -\dfrac{r^{d_c}_{d_c,z}}{I_{d_c,11}} & 0 & \dfrac{r^{d_c}_{d_c,x}}{I_{d_c,33}} \\[2ex] \dfrac{r^{d_c}_{d_c,y}}{I_{d_c,11}} & -\dfrac{r^{d_c}_{d_c,x}}{I_{d_c,22}} & 0 \end{bmatrix} \tag{35}$$

B_{62} is similar to B_{61} but with the target inertia and docking port position and B_{63} has the usual $1/m_c$ form where m_c is the chaser mass.

The state-space model described by (32) and (33) can be used to define control laws and will be used here inside the navigation filters. As the chaser and target control torques appear explicitly, that state-space model could be used for the design of a feedback-law that would control both the chaser and target at the same time. However, for operational reasons, it is desirable to keep the target GNC independent from the chaser. A reduced dynamics state-space model can be obtained by removing the target relative attitude from (32) and (33):

$$A_r = \begin{bmatrix} 0 & A_{12} & 0 & 0 \\ A_{21} & A_{22} & 0 & 0 \\ 0 & 0 & 0 & I_3 \\ A_{61} & A_{62} & A_{65} & A_{66} \end{bmatrix} \tag{36}$$

$$B_r = \begin{bmatrix} 0 & 0 \\ B_{21} & 0 \\ 0 & 0 \\ B_{61} & B_{63} \end{bmatrix} \tag{37}$$

The new state vectors is $\boldsymbol{x} = [\boldsymbol{\alpha}^{d_c d_t}, \boldsymbol{\omega}^{d_c d_t}_{d_c}, \boldsymbol{s}^{d_c d_t}_{d_t}, \dot{\boldsymbol{s}}^{d_c d_t}_{d_t}]^{\mathrm{T}}$ and the control input $\boldsymbol{u} = [\boldsymbol{T}_{d_c}, \boldsymbol{F}_{d_c}]^{\mathrm{T}}$, The main drawback of doing so is that the direct influence of the target state on the relative state is partially lost. However, the divergence at $\beta = \pm\pi/2$ previously mentioned for the 1-2-3 Euler sequence disappears as it was only appearing in the target attitude dynamics. This reduced state-space model can thus be used for any relative position/rotation as the target attitude can be linearised around any angle. Furthermore, it should be noted that even if the target attitude state was removed from the state-space, some of its information still remains available, for example in (34), which appears in (36).

Before deriving the measurement equations required for the navigation, the linearisation accuracy will be provided. The initial conditions for the simulation are as follow: the target docking port is rotated by 50 deg around each axis. The chaser is aligned with the target port and is positioned 10 m away. In the orbital frame, the chaser has the position $[-4.3 - 8.6 - 2.7]^{\mathrm{T}}$ m and is thus not at an equilibrium point and will start drifting. Fig. 5 and Fig. 6 show the relative position with the feed-forward term and without. With the feed-forward terms, which represents the constants coming from the linearisation, the error after 600 s is 5 cm. Without it, the error grows to 16 cm.

The feed-forward term in this configuration corresponds to 0.1 µN-m and 1 µm/s^2. This value is of the same order of magnitude as the environmental perturbations acting on the satellites and can thus be safely neglected.

3.3. Measurement equations

In this section, the measurement equations for the chaser relative position/rotation with respect to the target will be derived.

The metrology system is composed of various LEDs and a visible camera. The basic measurement equation when observing features using a camera is given by [1, p.272]:

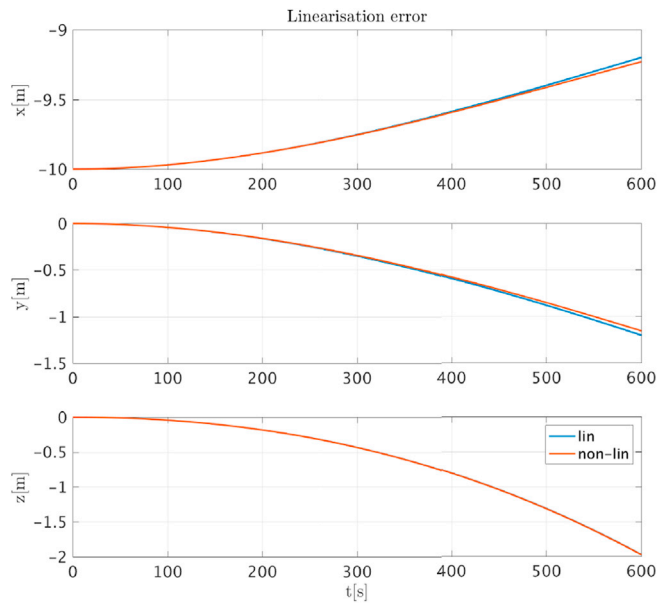[1] All the matrix elements are 3×3 matrices.

Fig. 5. Port to port position for the linearised and non-linear dynamics. The linearised dynamics includes the feed-forward terms.
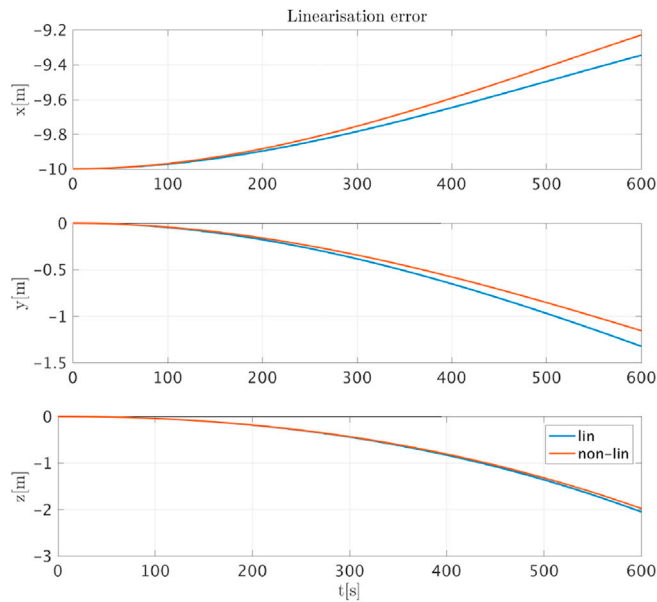

Fig. 6. Port to port position for the linearised and non-linear dynamics. The linearised dynamics does not include the feed-forward terms.

$$R = D\frac{f}{d} \tag{38}$$

where R is the range, D is the known size of the feature, f the focal length of the camera and d the feature size measured on the camera focal plane. The measurement error on a camera is typically one pixel (even though sub-pixel resolution can be obtained by defocusing the image [1, p.274]). Thus, to keep the error within the navigation performance requirements, the size of the pattern observed by the camera has to be increased with the range. Two different sets of LEDs are thus used depending on the range. Further more (38) does not take into account for perspective effect due to relative rotations. In order to get the true range, the image of the patterns needs first to be corrected by the relative attitude.

Fig. 7 shows the two patterns used. The central pattern is a cross composed of 5 LEDs with the central LED out-of-plane. All the LEDs are at
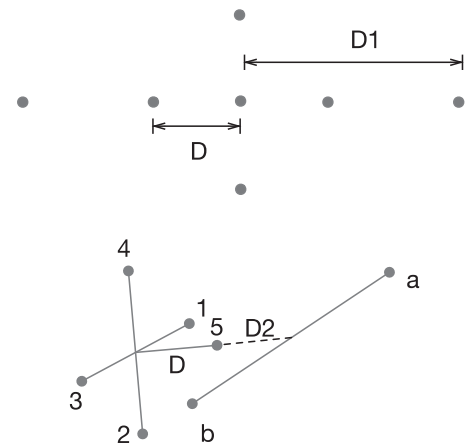
Fig. 7. The central pattern is composed of LEDs 1 to 5, with the 5th LED attached to the centre of the pattern and out-of-plane. The outer pattern is composed of LEDs a and b, together with the 5th LEDs of the central pattern. LEDs a and b are not laying in the same plane as the central pattern and are at a distance D_2 from LED 5.

a distance D from the centre. The outer pattern LEDs are at a distance D_1 from the centre and lay in a plane located at a distance D_2 from LED 5. As explained in Ref. [18], only two in-plane LEDs and one out-of-plane are necessary to solve the 6 DoF problem. However, a 5 LEDs cross pattern increases the robustness of the system in case of an LED failure and allows to have an analytical solution. Furthermore, circular patterns have the great advantage that their centre position is not affected by perspective effect. The drawback of the symmetry is that it is not possible to determine unambiguously rotations around the roll axis which are larger than $\pm\pi/2$ and the out-of-plane LED constraints the integration on the Cube-Sat. The discrepancy appearing for $\pm\pi/2$ could be easily solved by adding a 6th LED but it was deemed not necessary here, as during the RVD sequence the roll angle is expected to be always smaller than $\pm\pi/2$.

Fig. 8 shows the pattern and the camera in their respective frames, located on the chaser and the target. The frames are named n_c and n_t and the dynamics involved is strictly the same than the one derived in section 3.2 for the docking ports. The sought parameters are the position of the chaser navigation frame with respect to the target one, $s_{n_t}^{n_c n_t}$, and the relative attitude $A_{n_c n_t}$.

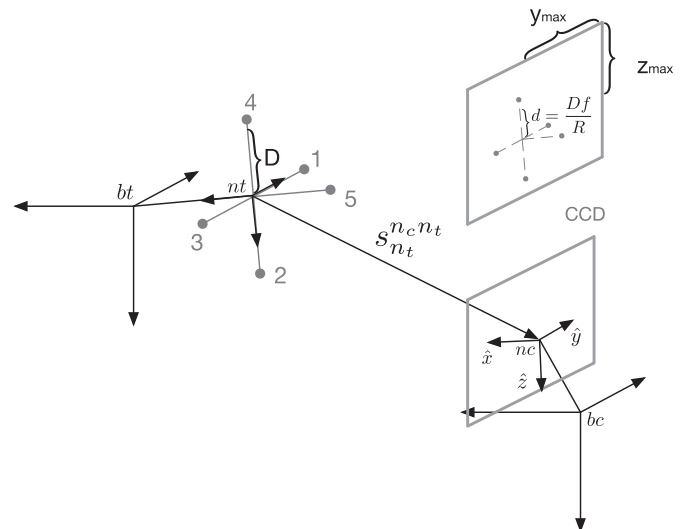From a crossed pattern and for small angles, as explained in Ref. [1]

Fig. 8. Vision Based Navigation problem scheme. The LED pattern is attached to the target navigation frame and the camera is to the chaser one.

and [20], the centre of the pattern provides the LoS angles and the position of the out-of-plane LED with respect to the centre gives the pitch and yaw relative angles, as shown in Fig. 9.

However, this approach does not picture the ambiguity between the rotations and the translations.

Fig. 10 shows how using the algorithms in Ref. [20] can lead to wrong results if the relative attitude and LoS angles are not small. "Small" should be understood such that the approximation $\sin(\alpha) \approx \alpha$ is valid, since in this assumption the rotation angles are decoupled from each other. Fig. 10a has the central LED aligned with the centre of the pattern. The pattern centre is however not aligned with the centre of the camera, corresponding then to a translation. This corresponds in fact to a chaser rotation. The same problem arises when the target is rotated. Because of the coupling, a target rotation corresponds to a rotation and a translation for the chaser, which cannot be identified when looking at Fig. 10b. In this case the rotation would first be detected and corrected. This would then lead to detecting a translation which could finally be performed. Finally, in Fig. 10c, a rotation and a translation would be detected even though this corresponds only to a translation of the chaser (a target translation would lead to an identical conclusion). A formulation of the problem which would allow to detect simultaneously the rotation and the translation would be more optimum as the corrections could then be achieved at the same time.
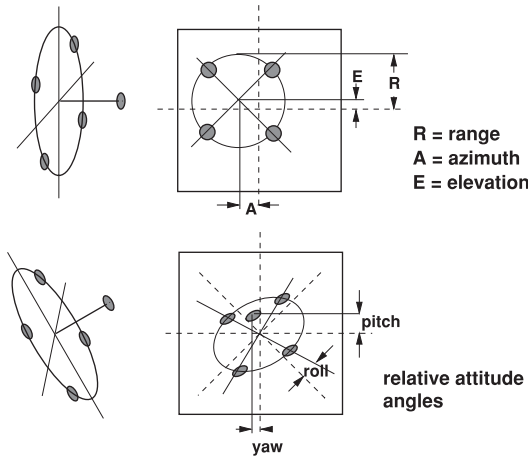
Fig. 9. Taken from Ref. [1]: Target pattern for a camera rendezvous sensor.

(a) Chaser rotation

(b) Target rotation

(c) Chaser translation
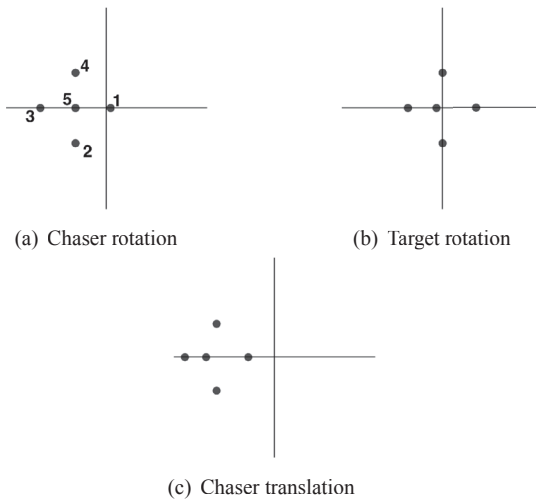
Fig. 10. a) shows the effect of a chaser rotation along its $+\hat{z}$ axis (according to the frame definition shown in Fig. 8). b) shows the same rotation but applied to the target. c) shows the effect of a chaser translation along $+\hat{y}$.

The measurement equations will be derived for the central LED pattern but can be directly applied to the outer LED afterwards. The informations known and available through the camera measurements are:

1. The known position of the ith LED in the target frame n_t, scaled down by the range R and focal length f (see Fig. 8): $\boldsymbol{x}_{n_t}^i$, $i = 1, \ldots, 5$. For example $\boldsymbol{x}_{n_t}^1 = [0\ 0\ Df/R]^{\mathrm{T}}$ and $\boldsymbol{x}_{n_t}^5 = [-Df/R\ 0\ 0]^{\mathrm{T}}$

2. The measured position of the ith LED in the chaser frame n_c, on the camera focal plane: $\boldsymbol{x}_{n_c}^i = [0\ p_y^i\ p_z^i]^{\mathrm{T}}$, $i = 1, \ldots, 5$. p_y and p_z are the LED position on the camera focal plane.

3. The position of the centre of the pattern in n_c: $\boldsymbol{x}_{n_c}^c = [0\ y^c\ z^c]^{\mathrm{T}}$.

The measurement equation can then be written:

$$\boldsymbol{x}_{n_c}^i = A_{n_c n_t}\boldsymbol{x}_{n_t}^i + \boldsymbol{x}_{n_c}^c \tag{39}$$

(39) describes the known position of the ith LED in the target frame n_t, scaled by the range R and focal length f. It is then transformed in the frame n_c and corrected by the position of the pattern centre, as shown on Fig. 11.

In order to be able to correct for the ambiguity between LoS and pitch/yaw rotations, the observed pattern needs first to be corrected by the roll angle. This facts constraints the Euler sequence which can be used. The measurement equations will be based on the 1-2-3 Euler sequence: $A_{n_c n_t}(\alpha, \beta, \gamma) = R_3(\gamma)R_2(\beta)R_1(\alpha)$.

$$\boldsymbol{x}_{n_c}^i - \boldsymbol{x}_{n_c}^c = A_{n_c n_t}(\alpha, \beta + El, \gamma + Az)\boldsymbol{x}_{n_t}^i \tag{40}$$

The relative attitude angles explicitly appear in (40) and the norm of $\boldsymbol{s}_{n_t}^{n_c n_t}$ is used in the definition of $\boldsymbol{x}_{n_t}^i$. For the first LED:

$$\boldsymbol{x}_{n_t}^1 = \begin{bmatrix} 0 \\ 0 \\ \dfrac{Df}{||\boldsymbol{s}_{n_t}^{n_c n_t}||^2} \end{bmatrix} \tag{41}$$

The centre position $\boldsymbol{x}_{n_c}^c$ needs to be related to $\boldsymbol{s}_{n_t}^{n_c n_t}$. This is done using the fact that in the camera focal plane, the LoS coordinates $[y^c\ z^c]^{\mathrm{T}}$ are:

$$\begin{cases} y^c = \tan(Az)\dfrac{y_{max}}{\tan(Az_{max})} \\ z^c = -\tan(El)\dfrac{z_{max}}{\tan(El_{max})} \end{cases} \tag{42}$$

where y_{max} and z_{max} are the size of the camera sensor and Az_{max} and El_{max} are the maximum value of the FoV along $+\hat{y}$ and $+\hat{z}$. The LoS angles are measured from the camera frame n_c towards the target frame n_t expressed in the frame n_c:
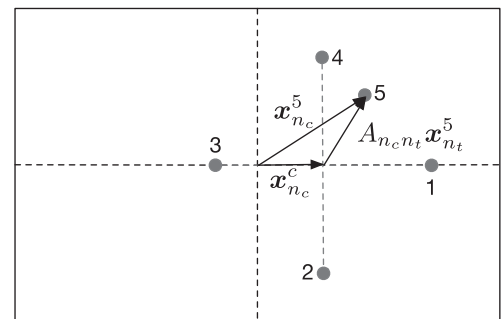

Fig. 11. The position of an LED on the camera sensor is the position of the pattern centre plus the transformed position the LED by the relative attitude matrix.

$$\begin{cases} \tan(Az) = \dfrac{\boldsymbol{s}_{n_c,y}^{n_t n_c}}{\boldsymbol{s}_{n_c,x}^{n_t n_c}} \\[2ex] \tan(El) = \dfrac{-\boldsymbol{s}_{n_c,z}^{n_t n_c}}{\left(\boldsymbol{s}_{n_c,x}^{n_t n_c 2} + \boldsymbol{s}_{n_c,y}^{n_t n_c 2}\right)^{1/2}} \end{cases} \qquad (43)$$

This can be related to the state variable $\boldsymbol{s}_{n_t}^{n_t n_c}$:

$$\boldsymbol{s}_{n_c}^{n_t n_c} = -A_{n_c n_t}(\alpha, \beta, \gamma)\boldsymbol{s}_{n_t}^{n_t n_c} \qquad (44)$$

The complete measurement equation for the ith LED can be written:

$$\boldsymbol{x}_{n_c}^{i} = A_{n_c n_t}(\alpha, \beta + El, \gamma + Az) \begin{bmatrix} 0 \\ 0 \\ \dfrac{Df}{\|\boldsymbol{s}_{n_t}^{n_t n_c}\|^2} \end{bmatrix} + \begin{bmatrix} 0 \\ \dfrac{\boldsymbol{s}_{n_c,y}^{n_t n_c}}{\boldsymbol{s}_{n_c,x}^{n_t n_c}} \dfrac{y_{max}}{\tan(Az_{max})} \\ \dfrac{\boldsymbol{s}_{n_c,z}^{n_t n_c}}{\left(\boldsymbol{s}_{n_c,x}^{n_t n_c 2} + \boldsymbol{s}_{n_c,y}^{n_t n_c 2}\right)^{1/2}} \dfrac{z_{max}}{\tan(El_{max})} \end{bmatrix} \qquad (45)$$

which is only a function of the state variables $[\boldsymbol{\alpha}^{n_c n_t}, \boldsymbol{s}_{n_t}^{n_c n_t}]^{\mathrm{T}}$. (45) can then be solved analytically to get the relative attitude and position or, can be used in an EKF.

This equation is also valid for the two outer LEDs using the appropriate distances D_1 and D_2 (see Fig. 7) and can be used all over the docking sequence. However, the distance D_2 of the 5th LED with respect the two outer LEDs will not be necessarily large enough to provide the required precision on the pitch and yaw angles determinations and thus on the range. For this reason, the two measurements of the chaser and target star trackers can be combined to get the relative attitude angles $\boldsymbol{\alpha}_{ST}^{n_c n_t}$ and an extra measurement equation can be obtained:

$$\boldsymbol{\alpha}_{ST}^{n_c n_t} = \boldsymbol{\alpha}^{n_c n_t} \qquad (46)$$

As the target star tracker measurement is necessary on-board the chaser, an active Inter-Satellite Link (ISL) is required between the two satellites.

3.4. Analytic navigation solution

Equation (45) provides a set of ten equations for six unknowns. This system is overdetermined and a priori no solution exists. An estimated solution could be obtained using a least squares method. However, the equations for LED 1 is minus than for LED 3. The same holds for LEDs 2 and 4. This symmetry in the system described by (45) can thus have an analytic solution.

The starting point for this algorithm is the coordinates of the five LEDs on the focal plane: $[p_y^i, p_z^i]^{\mathrm{T}}$, $i = 1, \ldots, 5$.

Using LEDs 1 to 4, the centre of the pattern can be obtained. As it is a cross, the centre is simply given by:

$$\begin{cases} y_c = \dfrac{1}{4}\sum_{i=1}^{4} p_y^i \\[2ex] z_c = \dfrac{1}{4}\sum_{i=1}^{4} p_z^i \end{cases} \qquad (47)$$

Each of the LED position on the camera sensor can now be expressed with respect to the pattern centre. For convenience, let's rename $\boldsymbol{x}_{n_c}^i - \boldsymbol{x}_{n_c}^c \equiv \boldsymbol{x}^{'i}$. $\boldsymbol{x}^{'i}$ has the general form:

$$\boldsymbol{x}^{'i} = \begin{bmatrix} 0 \\ \boldsymbol{x}_y^{'i} \\ \boldsymbol{x}_z^{'i} \end{bmatrix} \qquad (48)$$

(45) has the following solution:

$$\begin{cases} \alpha = \tan^{-1}\left(-\dfrac{\boldsymbol{x}_z^{'1}}{\boldsymbol{x}_z^{'2}}\right) \\[2ex] \gamma + Az = \sin^{-1}\left(-\dfrac{\boldsymbol{x}_y^{'5}}{\boldsymbol{x}_z^{'4}}\cos(\alpha)\right) \\[2ex] \beta + El = \sin^{-1}\left(\dfrac{\cos(\gamma + Az)\cos(\alpha)}{\boldsymbol{x}_y^{'3}\big/\boldsymbol{x}_z^{'5} + \sin(\gamma + Az)\sin(\alpha)}\right) \end{cases} \qquad (49)$$

It can be seen that the angles $\gamma + Az$ and $\beta + El$ cannot be obtained when a roll rotation of $\pi/2$ is performed as (49) diverges in this case. The range R is then given by:

$$R = \dfrac{Df}{\boldsymbol{x}_y^{'1}}(\cos(\alpha)\cos(\gamma + Az) - \sin(\alpha)\sin(\gamma + Az)\sin(\beta + El)) \qquad (50)$$

The LoS angles can be computed using the pattern centre position (47) and (42), and the attitude angles γ and β can be obtained.

Finally $\boldsymbol{s}_{n_t}^{n_c n_c}$ can be computed by first building the vector $\boldsymbol{s}_{n_c}^{n_c n_c}$ using the range, azimuth and elevation and transforming it back to the n_t frame:

$$\boldsymbol{s}_{n_t}^{n_c n_c} = -R_{123}^{\mathrm{T}}(\alpha, \beta, \gamma)\boldsymbol{s}_{n_c}^{n_c n_c} \qquad (51)$$

This algorithm has the great advantage of providing an explicit access to the navigation solution. It will however not work if one of the 5 LEDs would fail or if roll rotations larger than $\pi/2$ would be performed. The latter is hopefully not expected for RVD. A filtered solution is then preferred as primary navigation layer, although the analytical solution could be used as a watchdog alongside with the EKF own covariance matrix to monitor the navigation filter potential divergence. The use of the analytical solution for the monitoring carries a risk, due to its higher noise density and should be carefully analysed. If it does, the analytical solution can be used as a contingency navigation mode to bring the chaser to a predefined safe hold-point, which is yet to be defined depending on mission and systems constraints.

3.5. Extended Kalman filter formulation

The Extended Kalman filter (EKF) presented here closely follows the formulation proposed by Ref. [29]. Fig. 12 gives its general structure.

In it's original formulation, the EKF performs the integration step of the state and covariance using the non-linear dynamics. However, as mentioned in section 3.2, the target CubeSat state variables are not accessible on-board the chaser. The reduced state-space model given by

Model	$\dot{\mathbf{x}}(t) = \mathbf{f}(\mathbf{x}(t), \mathbf{u}(t), t) + G(t)\mathbf{w}(t), \ \mathbf{w}(t) \sim N(\mathbf{0}, Q(t))$
	$\tilde{\mathbf{y}}_k = \mathbf{h}(\mathbf{x}_k) + \mathbf{v}_k, \ \mathbf{v}_k \sim N(\mathbf{0}, R_k)$
Initialize	$\hat{\mathbf{x}}(t_0) = \hat{\mathbf{x}}_0$
	$P_0 = E\left\{\tilde{\mathbf{x}}(t_0)\,\tilde{\mathbf{x}}^T(t_0)\right\}$
Gain	$K_k = P_k^- H_k^T(\hat{\mathbf{x}}_k^-)[H_k(\hat{\mathbf{x}}_k^-)P_k^- H_k^T(\hat{\mathbf{x}}_k^-) + R_k]^{-1}$
	$H_k(\hat{\mathbf{x}}_k^-) \equiv \left.\dfrac{\partial \mathbf{h}}{\partial \mathbf{x}}\right\|_{\hat{\mathbf{x}}_k^-}$
Update	$\hat{\mathbf{x}}_k^+ = \hat{\mathbf{x}}_k^- + K_k[\tilde{\mathbf{y}}_k - \mathbf{h}(\hat{\mathbf{x}}_k^-)]$
	$P_k^+ = [I - K_k H_k(\hat{\mathbf{x}}_k^-)]P_k^-$
Propagation	$\dot{\hat{\mathbf{x}}}(t) = \mathbf{f}(\hat{\mathbf{x}}(t), \mathbf{u}(t), t)$
	$\dot{P}(t) = F(\hat{\mathbf{x}}(t), t)P(t) + P(t)F^T(\hat{\mathbf{x}}(t), t) + G(t)Q(t)G^T(t)$
	$F(\hat{\mathbf{x}}(t), t) \equiv \left.\dfrac{\partial \mathbf{f}}{\partial \mathbf{x}}\right\|_{\hat{\mathbf{x}}(t)}$

Fig. 12. Taken from [29, p.289]: Continuous-Discrete Extended Kalman Filter.

(36) and (37) has to be used and a discrete propagation method has to be applied.

$$\widehat{\boldsymbol{x}}_{k+1}^- = F_k \widehat{\boldsymbol{x}}_k^+ + B_k \boldsymbol{u}_k \tag{52}$$

$$P_{k+1}^- = F_k P_k^+ F_k^{\mathrm{T}} + Q_k \tag{53}$$

where F_k is the state transition matrix. In (45), the measurement equation $\boldsymbol{y}_k = \boldsymbol{h}(\boldsymbol{x}_k)$ was described. For the calculation of the Kalman gain, the Jacobian $H_k = \partial_{\boldsymbol{x}_k} \boldsymbol{h}(\boldsymbol{x}_k)\big|_{\widehat{\boldsymbol{x}}_k}$ evaluated at the current estimate is required. It was computed using the MATLAB Symbolic toolbox. The expression of H_k being extremely long, it will not be shown here. A special care should be taken for the update equations as some of the components of the measurement equations or of the state vector are Euler angles and are thus not additive. This can be simply done using matrices:

$$R_{123}(\alpha^+, \beta^+, \gamma^+) = R_{123}(\Delta\alpha, \Delta\beta, \Delta\gamma) R_{123}(\alpha^-, \beta^-, \gamma^-) \tag{54}$$

The EKF will also be used to propagate the state vector in case of sensor loss and to actively track the LEDs using the a posteriori estimate of the state at $k+1$, thus increasing the VBN robustness to undesired signals on the camera sensor, caused by the Sun or the Earth.

Two different EKF are used:

1 The first filter will use the outer LEDs and the central one combined with the star tracker measurements that the chaser and target are providing. This filter is used from 10 m range until 5 m range.
2 The second filter will rely only the 5 LEDs of the central crossed pattern and will be used from 5 m range until docking.

The process noise diagonal matrix involved in the filtering process has the following structure:

$$Q_k = \mathrm{diag}\begin{bmatrix} \sigma_\alpha^2 & \sigma_\omega^2 & \sigma_s^2 & \sigma_{\dot{s}}^2 \end{bmatrix} \Delta t \tag{55}$$

with Δt the filter sampling time. The attitude angles and the position are uniquely determined by their respective dynamics. Given an initial condition, their value can obtained respectively integrating directly the rotation rate and the velocity. Thus $\sigma_\alpha^2 = \sigma_s^2 = 0$. σ_ω^2 and $\sigma_{\dot{s}}^2$ will need to be tuned to achieve the required filter accuracy.

Because of the uncertainties in the dynamics used to fine-tune the process noise matrix, an adaptation estimation of Q might be useful. This is proposed in Refs. [30] and [31]. The estimated noise is:

$$\widehat{Q}_k^+ = \widehat{Q}_k^- + \frac{1}{L_Q}\left(Q^* - \widehat{Q}_k^-\right) \tag{56}$$

where

$$Q^* = \left(\widehat{x}_k^+ - \widehat{x}_k^-\right)\left(\widehat{x}_k^+ - \widehat{x}_k^-\right)^{\mathrm{T}} + P_k^- - P_k^+ - \widehat{Q}_k^- \tag{57}$$

and L_Q is a parameter which has to be manually selected. The necessity of using an adaptation Q will be assessed by testing the robustness of the EKF to uncertainties and unmodelled dynamics.

The input to the filter are the forces and torques computed by the controller. These input commands are different than the ones executed by the satellite because of the various sources of error such as attitude and thrust error, or centre of gravity position uncertainties. At this level of design, only the attitude errors were considered. The other sources will contribute to degrading the navigation solution and shall be investigated in future work.

3.6. VBN hardware

The sizing of the outer LED pattern is driven by the fact that the docking system (docking mechanism and metrology system) shall fit in a 1 unit CubeSat surface, i.e 10×10 cm^2, constraining $D_1 = 5$ cm (Fig. 7).

The inner pattern dimension was designed to have sufficient accuracy at a 5 m range, when the handover between the outer and inner patter is performed, but also to be able to observe it from 5 m range down to docking, with an optics that would not have to be a fish-eye avoiding then radial and tangential distortions. This led to a distance $D = 2$ cm.

No dedicated RVD sensor exists yet for CubeSats. As it is usually the case for CubeSats missions, Commercial Off-The-Shelf (COTS) hardware is preferred in order to keep the costs low. The COTS mono-chromatic Basler ACE camera acA3800-10 gm [32] was chosen. With a sensor of 2764×3856 pixels and a pixel size of $1.67\ \mu m$, an optics with a 4 mm focal length was selected. Due to its very small size and weight, it can be easily integrated on a CubeSat. The camera with the selected optics has a total FoV ≈ 60deg. It will be placed 4 cm inside the CubeSat structure and the crossed LED pattern will be 3 cm inside the CubeSat. The two outer LEDs are position on the external structure itself. Fig. 13 shows the hardware disposition and dimensions.

Consequently, when the two CubeSats are docked, the camera is 7 cm away from the central pattern which ensures that it remains visible during the whole approach until docking.

The camera sensor has its peak quantum efficiency at 460 nm. LEDs emitting in the blue part of the spectrum were thus selected. To minimize the stray light from the Sun, a bandpass filter is used on the optics. The filter peak transmission is at 470 nm [33]. The selected LEDs have a peak emission at 470 nm, a viewing angle of 80 deg and a luminous intensity of 1.2 cd.

Note that using a colour camera and coloured LEDs would allow to solve the roll ambiguity mentioned earlier. However, in order to keep the camera data rate low and as large roll angles are not expected, the monochromatic solution was preferred. Furthermore, the bandpass filter used on the optics would need to be modified to cope with multiple wavelengths which means that the camera would be more sensitive to external illumination conditions.

3.7. LED detection and tracking

To keep the computational load as low as possible, the only vision algorithm used is the Blob analysis of the MATLAB Computer Vision System toolbox. This algorithm detects connected regions (blobs) on a binary image and output the centroid of each blobs. The centroids co-ordinates are then used in the EKF (45) or in the analytical solution described in section 3.4. The binary image is obtained by thresholding the raw image. Because the LEDs are active, the minimum integration time of the camera can be obtained such that the centre of the LEDs does not saturate the sensor at 10 m. Fig. 14 shows the image produced by the camera with an exposure time set to 35 μs.
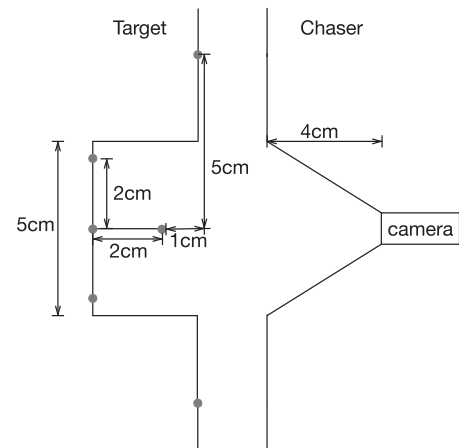

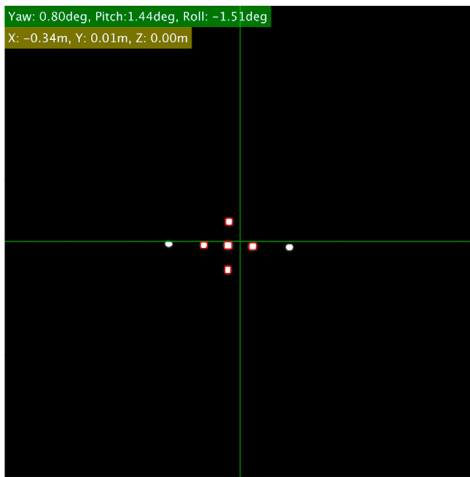**Fig. 13.** Position of the 2 LED patterns and camera in the target and chaser structures.

Fig. 14. Real image obtained by the camera observing the LEDs at a range of ∼ 34 cm. The relative 6 DoF were obtained using the analytical solution.

The active tracking of the LEDs is done by using the measurement equation (45) and the navigation filter a posteriori estimation at $k + 1$ to obtain the estimated position of the LEDs within a certain confidence interval, given by the EKF covariance. It allows as well to define a Region of Interest (ROI) on the image obtained by the camera which will decrease the number of pixels that the connected region algorithm will have to analyse, but mainly, windowing the image will reduce the number of parasite signals that the camera may detect and will decrease the stray light. This ROI is in fact the confidence interval defined using the estimated covariance matrix of the EKF.

Two cases have to be considered:

1. The VBN has converged and its precision allows the active tracking of the LEDs. If n LEDs have to be observed ($\boldsymbol{x}_{n_c}^i$) and that m connected regions are detected ($\boldsymbol{x}_{\text{blob}}^j$), $m > n$, n connected regions among m regions detected need to be selected. Knowing the a posteriori position of each LED, provided by the EKF ($\widehat{\boldsymbol{x}}_{n_c}^i$), the norm between each estimate and each signal can be computed $\left\| \widehat{\boldsymbol{x}}_{n_c}^i - \boldsymbol{x}_{\text{blob}}^j \right\|$ for $i = 1, \ldots, n$ and $j = 1, \ldots, m$. The n connected regions which are the closest to an a posteriori position will then be selected.

2. If the VBN was not initialised yet or if the precision is deemed not satisfying, active tracking of each LED cannot be performed. This can be solved by using the geometrical properties of the two patterns.

Determining the precision of a navigation filter on orbit is not an easy task. If the central 5 LEDs pattern is observed, the precision can be assessed using the analytical formulation as this represents a raw (i.e. noisy) solution. For both patterns, the EKF provides a confidence interval on the LEDs positions for the next time step. Also, the number of pixels between two neighbour LEDs can be measured directly on the camera sensor. Thus, if an LED confidence interval is greater than half the measured distance in pixels between two nearest neighbour LEDs, the EKF is deemed not precise enough as the confidence intervals of each LEDs may overlap. If this happens, the geometrical features are used. Finally, as the geometrical features algorithm uses only simple operations, it will always run in parallel to the EKF, adding an extra layer of robustness for the LEDs detection as this is a critical aspect of the navigation.

3.7.1. LEDs patterns geometrical features

Because the two patterns have fixed geometrical properties, features can easily be extracted.

Fig. 15 shows the features for the external and internal patterns. For

(a) External pattern   (b) Internal pattern
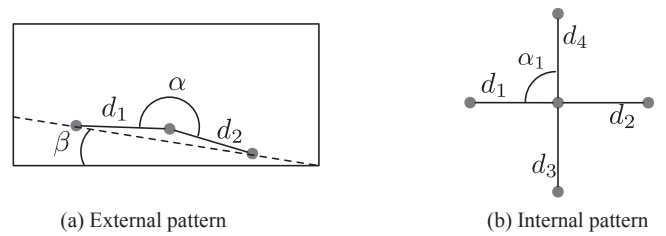
Fig. 15. Geometrical features of the two different LED patterns. Only range invariant features were selected.

the external patterns, the angle α is expected to be always close to π. This angle will of course vary due to the perspective effects caused by control and navigation errors. However, the maximum expected attitude errors are known and thus ranges of values for α can be predicted. The distance ratio between the outer LEDs and the central LED, d_1/d_2, is expected to be always close to unity. The pattern should be always aligned with the camera sensor horizon, thus β is expected to be close to zero. Finally, the expected maximum number of pixels between the two outer LEDs was added as an extra features. The upper bound for this value is given at 5 m and the lower bound at a 10 m range.

For the central pattern, the features extracted are similar than for the outer pattern. The features are the four length ratios d_1/d_2, d_1/d_3, d_2/d_4 and d_3/d_4, and the orthogonality between the LEDs α_i, $i = 1, \ldots, 4$. Finally, the ratio $(d_1 + d_2)/(d_3 + d_4)$ is provided. The signals are analysed by forming groups of 5 blobs.

To differentiate reflections and undesirable signals from LEDs signals, among all the detected connected regions on the camera sensors (blobs), groups of three blobs are constructed for the external pattern (groups of five blob for the internal one). For each group the features are extracted and tested against the expected values that can be computed using the expected GNC accuracy. If the features are within the expected bounds, the LEDs are considered detected.

Fig. 16 shows a sample image.

The true LEDs signals were generated based on the expected GNC accuracy. Reflections were simulated by randomly generating blobs of white pixels. Simulation shows that the true signals can be unambiguously detected. The algorithm was then tested more rigorously using an experimental set-up, as explained in the next section.

4. Results

Before showing the results, the controller used to assess the VBN performance will be briefly introduced. The chosen controller is a Linear Quadratic Regulator because of its guaranteed phase and gain margins. If coupled to a Kalman filter, a Linear Quadratic Gaussian control (LQG) is obtained for which the good frequency properties of the LQR cannot be
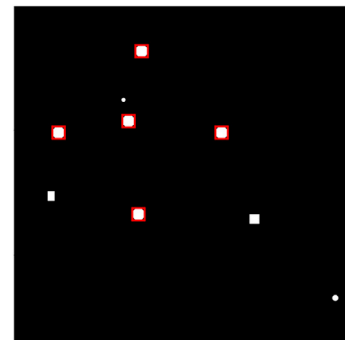

Fig. 16. Sample image simulated. The LEDs are recognized and marked in red. (For interpretation of the references to colour in this figure legend, the reader is referred to the Web version of this article.)

guaranteed any more [34]. The LQG stability will not be discussed here as the aim is to assess the performance of the VBN and not the robustness of the closed-loop GNC which is planned to be addressed in a later paper. Furthermore, the stability of the EKF can be analysed without considering the controller by means of the separation theorem [29]. The LQR cost function is given by:

$$J = \int_0^\infty \mathrm{dt}\, (\boldsymbol{x}^\mathrm{T} Q \boldsymbol{x} + \boldsymbol{u}^\mathrm{T} R \boldsymbol{u}) \tag{58}$$

and the Q and R matrices were selected as:

$$Q = \begin{bmatrix} 3.28 \cdot 10^5\, I_3 & 0 & 0 & 0 \\ 0 & 3.28 \cdot 10^5\, I_3 & 0 & 0 \\ 0 & 0 & 10^4\, I_3 & 0 \\ 0 & 0 & 0 & 10^4\, I_3 \end{bmatrix} \tag{59}$$

$$R = \begin{bmatrix} 2.5 \cdot 10^9\, I_3 & 0 \\ 0 & 2.5 \cdot 10^5\, I_3 \end{bmatrix} \tag{60}$$

The feed-forward terms due to the linearisation are not added explicitly in the control loop. The LQR will thus need to add constant corrections to maintain a desired position and attitude. Adding an integrator was not deemed necessary as the steady sate error is only 0.5 mm at 10 m range and 0.03 mm at 1 m range.

The EKF and LQR are both sampled at 1 Hz. The maximum thrust per axis is set to 4 mN, provided by a miniaturised propulsion system, and the torque capability per axis is 2 mN-m. Note that no actuator noise disturbance is considered here.

The target is assumed to be on a 600 km altitude, 6AM Sun Synchronous Orbit (SSO). Its Attitude Determination & Control System (ADCS) is the same than the one described in Ref. [21]. Its star tracker being always available (nominal scenario), the 3 σ control accuracy is ∼ 0.5 deg around each axis.

The guidance profiles are shown in Fig. 17. The acceleration is set to use a maximum of 2 mN of thrust. This way, the actuators are not in saturation.

The chosen Q and R matrices of the LQR give an aggressive controller. This may not be required by the mission itself. But as the aim here is to assess the performances of the navigation filters, an aggressive controller ensures then good tracking and negligible steady state error, as discussed before. The controlled relative position and attitude are thus reflecting the real performances of the navigation.

The following sections will discuss the VBN in the case where the target docking port is rotated by 50 deg around each axis and the chaser port face is parallel to the chaser external structure. In this case, when the chaser is aligned with the target docking port axis, it is not at an equilibrium position. Consequently, the constant terms that were neglected during the linearisation will have to be compensated by the LQR for the control and by the process noise for the EKF.

For both cases, the docking ports in the chaser and target body frame have the following coordinates:

$$\begin{cases} \boldsymbol{r}_{b_t}^{d_t} = \begin{bmatrix} -0.1 & 0.1 & 0.1 \end{bmatrix}^\mathrm{T} \\ \boldsymbol{r}_{b_c}^{d_c} = \begin{bmatrix} 0.1 & 0.1 & 0.1 \end{bmatrix}^\mathrm{T} \end{cases} \tag{61}$$

The navigation LEDs and sensors are in the centre of the docking port but pulled back by 3 cm in target and 4 cm in the chaser respectively, according to Fig. 13. To assess the performances of the image processing and the EKF, a simple camera model was developed. It allows to simulate the LED signals on the camera sensor including measurements errors, simulated as a Gaussian white noise. Several measurements, using the actual camera, at ranges of 10 m, 5 m and 1 m show that the noise level on the camera sensor is of the order of $3 \cdot 10^{-2}$ pixels. This accuracy can be explained by the fact that the optics is never focused exactly on the LEDs as the camera working range varies between 10 m and 7 cm and is not equipped with an auto-focus. This allows to obtain a desired blurring effect, allowing a sub-pixel resolution [1, p.274].
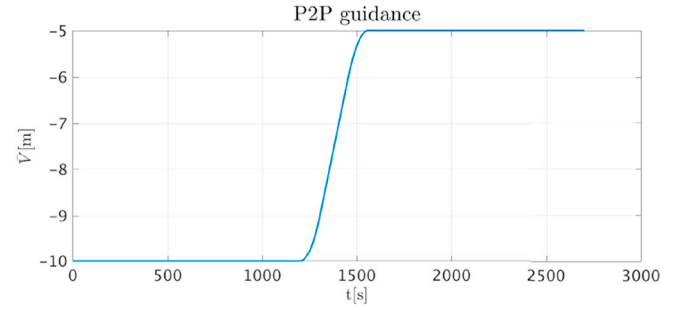
(a) 10 m to 5 m range
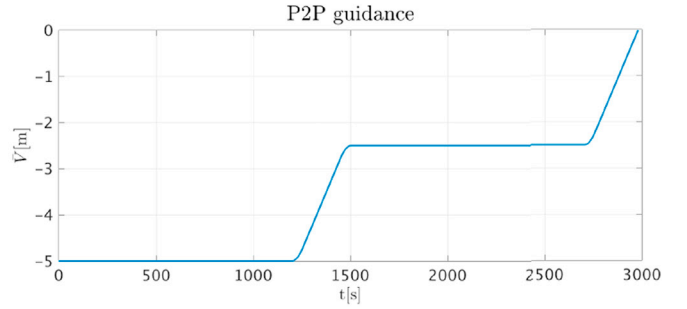
(b) 5 m range to docking

Fig. 17. a) Guidance profile from 10 m to 5 m. The translation speed is set to 0.02 m/s b) Guidance profile from 5 m until docking with a hold point at 2.5 m. The translation speed is set to 0.01 m/s.

The EKF parameters were set as follow: $\sigma_{\dot{s}} = \sigma_\omega = 5 \cdot 10^{-6}$. This is consistent with the linearisation feed-forward term which was neglected and with the level of orbital perturbations that can be expected for CubeSats at the assumed altitude. The noise measurement matrix R is composed of the LED measurement noise and star tracker noise. The LED noise is $\sigma_{\mathrm{LED}} = 3 \cdot 10^{-2}$ (in pixels unit), as explained previously. The star tracker noise is set to $\sigma_{\mathrm{ST}} = 4 \cdot 10^{-4}$ rad. This is assuming the ST-200 star tracker [35]. The initial covariance matrix P_0 was set to $P_0 = 10^{-4} I_{12}$.

4.1. 10 m range: 3 LEDs and star trackers

At this range, the two outer LEDs and the central one are used in

combination with the chaser and target star tracker measurement.

4.1.1. Handover

When the chaser arrives at point S_3, it is navigating using CDGPS (10 cm accuracy) and an ADCS similar to the target one. The VBN needs to be initialised and it can only be performed if the star trackers measurements are available. Considering the ADCS and CDGPS errors, an estimate of the LEDs position can be obtained as shown on Fig. 18. If no perturbations is detected in this ROI, then the detection of the 3 signals is an easy task. However, if after thresholding the image, more than 3 connected regions are detected, the geometrical features are used. Figs. 18 and 22 are not showing the full camera sensor but are zoomed in order to see the signals as the two outer LEDs are only separated by ∼24 pixels.

To assess the performances of the algorithm using the geometrical features of the patterns, the face of a 6 Units CubeSat was created, as shown on Fig. 19. It has dimensions 20 cm by 30 cm and is composed of a black anodized aluminium structure covered with an FR4 PCB. On the PCB, solar cells mock-up were glued as well as two patch antennas and two sun sensors. The docking mechanism is supposed to be in between the inner pattern and outer pattern and was not included here as it is assumed it will be covered with an anti-reflective coating. The CubeSat panel was illuminated using a Sun simulator and observed using the camera.

Due to the fact that the camera is using a very short exposure time, no reflections or stray-light were detected, for any relative position/angle between the LEDs, the camera, and the Sun. A measurement campaign was then performed with the Sun in the FoV of the camera. at ranges of 10 m, 5 m and 1 m. The algorithm using the geometrical features could always successfully reject the Sun as shown on Fig. 20 and Fig. 21. The noise on the LEDs was only marginally impacted by the Sun. This will still
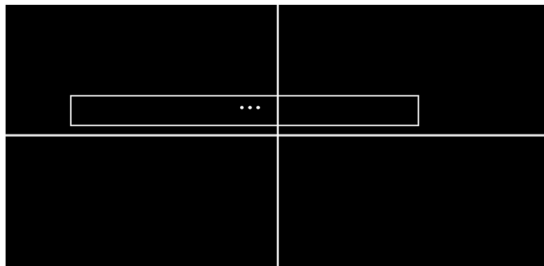
Fig. 21. Central LEDs pattern detection at 1 m range with the Sun simulator in the camera FoV.

be taken into account to assess the robustness of the navigation solution. Note that no motion blur was observed during the test campaign. This was expected due to the very short exposure time. Assuming a relative motion of 0.1 deg/s, the scene observed with the camera is moving by only $\approx 1.5 \times 10^{-4}$ pixels during each exposure.

The described experiment and its results give confidence that the navigation algorithm can successfully be initialised and is robust to any illumination conditions, even if the Sun is in the camera FoV. The Earth impact was not treated during this experiment. But as its luminosity is lower than the Sun, it is assumed that the Earth can be successfully rejected if it is in the camera FoV, using the same algorithms. The docking can thus take place at any time, on any orbit provided that both star trackers and CDGPS are available during the handover. Once the filter has converged, the 3σ a posteriori estimated position of the LEDs is precise enough to stop using the geometrical features algorithm and actively track the LEDs as the Sun or the Earth will not be inside the ROI, as shown on Fig. 22.

4.1.2. Performance

The following results show the behaviour of the VBN during the forced translation from 10 m range to 5 m range. The time line of the simulation is the following:

1. 0–600 s: VBN initialization. Filter is out of the control loop.
2. 600 s–1200 s: Include VBN in the control loop.
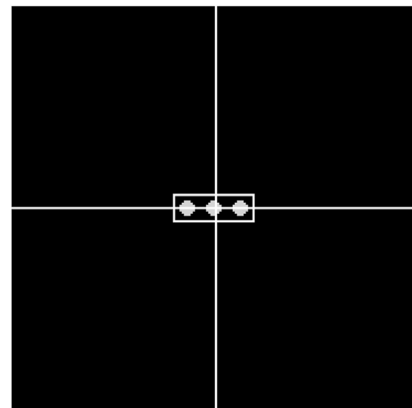3. 1200 s–1560 s: Forced motion from 10 m to 5 m range at 0.02 m/s.

Fig. 18. Estimated regions of the LEDs position, based on the CDGPS and ADCS accuracy (3σ).

Fig. 19. 6U front panel mock-up.

Fig. 20. Outer LEDs pattern detection at 10 m range with the Sun simulator in the camera FoV.

Fig. 22. Estimated regions where the LEDs position, using the EKF a posteriori estimate (3σ).

4. 1560 s–2700 s: Station keeping at 5 m range.

For attitude determination and control, the rule of thumb is that the determination should be ∼ 10 times better than the required pointing accuracy, or approximately 0.2 deg around each axis. For relative position estimation, the accuracy should be 1% of the range or better [1, p.20].

Fig. 23 shows the Port to Port (P2P) EKF error. The notation $\overline{V}$, $\overline{H}$ and $\overline{R}$ are here used to describe the x, y and z directions in the docking port frame. The attitude determination error is constant over the approach as the measurements are provided by the star trackers. As stated in section 2, the relative attitude pointing shall be better than 2 deg around each axis. On Fig. 23, the relative attitude estimation is better than 0.1 deg around each axis. Which means that the relative pointing accuracy would be of the order of 1 deg.

The relative position estimation will improve over the trajectory as it can clearly be noticed on Fig. 23. Along the approach trajectory, the error remains well below the 1% accuracy as seen on Fig. 24. This is important to gain confidence that when actuators errors will be included in the loop and finally on-orbit, the performances should still be within the requirements. Note that the filter has converged in less than 5 min. The bias that can be noticed on Fig. 23 is an effect of the residual dipole inside the
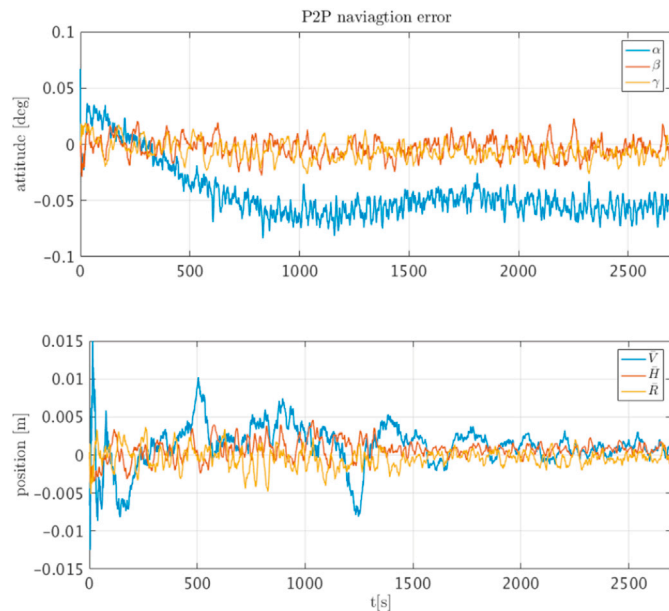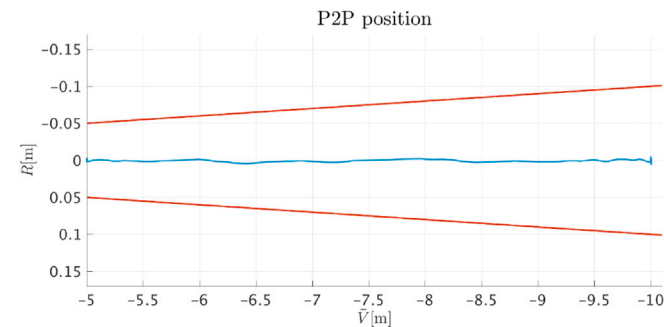
CubeSat and other environmental perturbations, and will be discussed at the end of this section.

If the star tracker measurements are lost, how is the filter behaving using only the three LEDs? In the following simulations, the filter was initialised with the star trackers, which were then lost at t = 800 s. The translation was thus performed using only the LEDs measurements.

The attitude estimation degrades to 0.4 deg around the yaw axis (Fig. 25). Using the 10 times rule of thumb would lead to a pointing accuracy of 4 deg. This is violating the 2 deg accuracy required for the docking. However, this happens at a range of 10 m, which may be acceptable. Furthermore, the performance including realistic actuator models will need to be performed at which point a comprehensive estimation of the pointing accuracy will be performed. This is not considered as a show stopper at this moment. A larger error in the trajectory can be observed. This is the impact of the relative attitude estimation error. However the position estimation is still better than the 1% accuracy.

When the star tracker are lost, the a posteriori estimation for the LEDs tracking is degraded. The active tracking is not reliable any more and the geometrical features algorithm has to be used as reflections may appear in the a posteriori ROI.

In the previous simulations, the nominal values of the satellites parameters were used. However, the masses and inertia tensors are expected to vary on the order of ±10%. Furthermore, the LEDs signal error on the camera sensor was measured in a laboratory and the effect of the space environment on the noise was not assessed. For this reason, the LEDs noise was allowed to vary by 50%. If the star tracker remains available, the EKF does not exhibit any problems. In the case of a star tracker loss, the filter clearly violated the 1% bound. Consequently, the adaptation process described in section 3.5 was used for the Q matrix. The parameter L_Q of equation (56) was set to 10^6 and is thus only marginally modifying the process noise, however enough to satisfy the accuracy requirement. Fig. 26 shows the result of 50 Monte-Carlo simulations. Note that to reflect only the EKF behaviour the uncertainties on the controller, the LQR gain was computed for each Monte-Carlo run. This way, the result only shows the navigation filter performance.

For the uncertainties which were considered, the EKF satisfies the accuracy requirements.
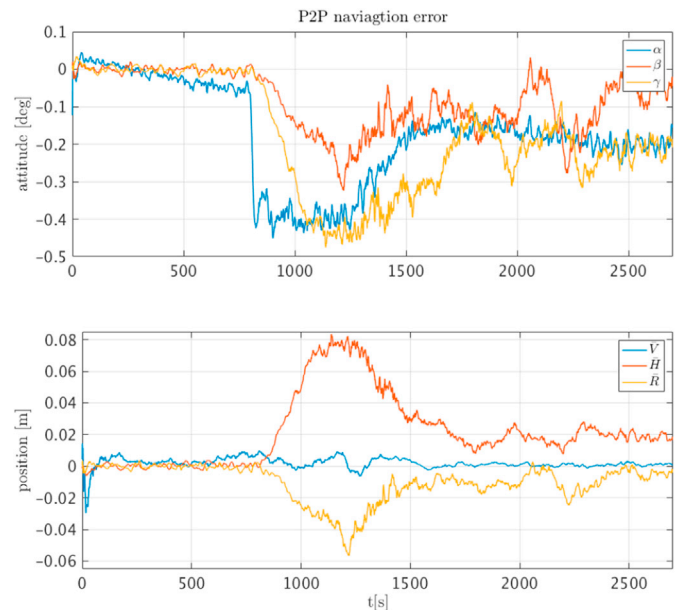

Fig. 23. Navigation filter output using 3 LEDs and the star trackers measurements. At t = 600 s, the EKF is included in the control-loop. At t = 1200 s, the translation begins.

Fig. 24. Relative position in the docking port frame. The red lines are the 1% of the range boundaries. As for the LVLH frame, $\overline{R}$ is along $\hat{z}$ and $\overline{V}$ along $\hat{x}$. (For interpretation of the references to colour in this figure legend, the reader is referred to the Web version of this article.)

Fig. 25. Navigation filter output using 3 LEDs and the star trackers measurements. At t = 600 s, the EKF is included in the control-loop. At t = 800 s, the star trackers are lost. At t = 1200 s, the translation begins.
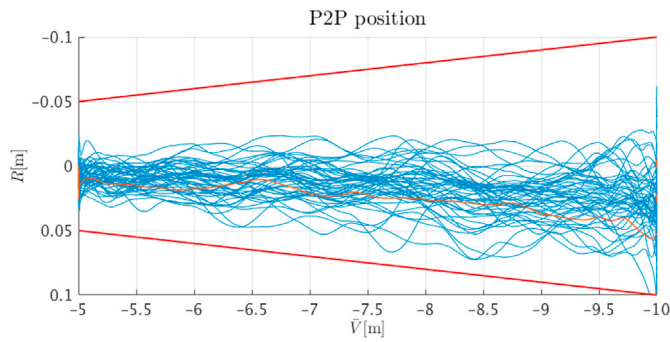
Fig. 26. Monte-Carlo simulation using 10% variation on the satellites masses and inertia tensors and 50% on the LEDs noise. The trajectory in orange shows the simulation with the nominal parameters. (For interpretation of the references to colour in this figure legend, the reader is referred to the Web version of this article.)

4.2. 5 m range: 5 LEDs

At this range, the central pattern can be observed and the 6 DoF solution can be fully obtained using only the LEDs signal. When arriving at 5 m range, the chaser is navigating using 3 LEDs pattern and the star trackers, and the handover to the 5 LEDs pattern needs to take place.

4.2.1. Handover
If the 3 LEDs EKF has access to the star trackers measurements, the accuracy of the filter is precise enough to estimate accurately the a posteriori position of the central pattern LEDs. The handover is then an easy task. Fig. 27 shows the a posteriori ROI.

If the star trackers are not available during the handover, the ROI is too wide and the geometrical features algorithm needs to be used. The detection is performed detecting first the five central LEDs and then, the outer two LEDs. As for the 3 LEDs plus star trackers case, once the navigation filter has converged, the LEDs can actively be tracked. The performances of the geometrical features algorithm was again assessed under the same configuration than previously described and stray light, the Sun and reflections can successfully be rejected and the LEDs are successfully detected, 100% of the time.

4.2.2. Performance
The following results will show the behaviour of the VBN during the forced translation from 5 m range to docking. The time line of the simulation is the following:

1. 0–600 s: VBN initialization. Filter is out of the control loop.
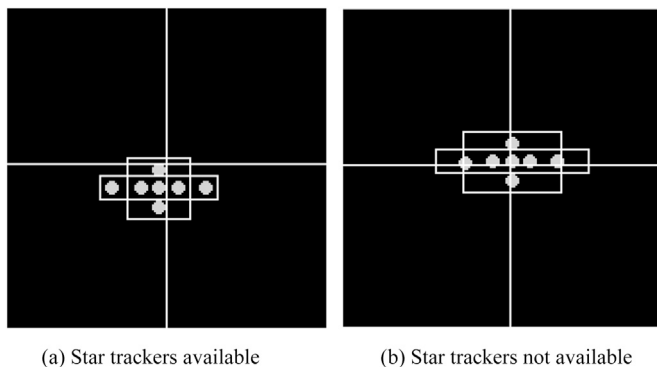2. 600 s–1200 s: Include VBN in the control loop.

3. 1200 s–1505 s: Forced motion from 5 m to 2.5 m range at 0.01 m/s.
4. 1505 s–2705 s: Station keeping at 2.5 m range.
5. 2705 s–2980 s: Forced motion from 2.5 m to docking at 0.01 m/s.

The accuracy of the filter will improve over the approach as the central crossed pattern covers a larger amount of pixels on the camera sensor, thus reducing the measurement error. A station keeping point at 2.5 m was introduced and allows for a better convergence of the navigation and a final systems check before the final translation. Fig. 28 shows the navigation performance all along the docking trajectory. A slight improvement of the navigation solution can be observed at the 2.5 m range station keeping point, between 1505 and 2705 s. This improvement will be more significant as actuator noise and control errors will be added in the simulations.

The attitude determination is 0.5 deg at 5 m and thus not compliant with the 0.2 deg determination. This is however not considered as a show stopper, as explained before. If required, the relative attitude estimation could be improved by using the star trackers measurements. It is however desirable to stop using the ISL required to transmit the attitude data as soon as possible to keep the power consumption low. Furthermore, depending on the systems and orbital configuration, it is not guarantee that the start trackers will be available at any time. At the moment of docking, the attitude error value was of the order of $5 \cdot 10^{-3}$ deg around each axis and exceeds the required determination accuracy. The position determination requirement should still be equal or better to 1% of the range during the approach. The docking requirement is 1.2 cm misalignment. The navigation output should then be of the order of 1 mm at docking. Fig. 29 shows this requirement (red lines) and the actual position of the chaser in the target docking frame. The accuracy on the relative state determination is clearly improving over the range, as expected, and achieves a navigation error better than 10^{-4} m at docking.

Fig. 30 shows the results of 50 Monte-Carlo runs using the same uncertainties than previously described. This Monte-Carlo run is independent from Fig. 26. Here, the adaptation of the process noise was not used. The chaser remains always well inside the 1% of the range accuracy envelope and shows the robustness of the filter to masses, inertia tensor and measurements noise uncertainties.

The analytical solution is provided on Fig. 31. This provides a raw 6 DoF solution i.e. with noise. The attitude standard deviation is ∼0.6 deg (3σ) at 5 m and improves until 0.003 deg around each axis at docking. For the position, the standard deviation is ∼0.05 m (3σ) at 5 m and improves

(a) Star trackers available   (b) Star trackers not available

Fig. 27. a) The 3 LEDs EKF has access to the star trackers and the central LEDs can be actively tracked. b) The precision of the filter does not allow reliable tracking and the geometrical features are used to reject parasite signals.
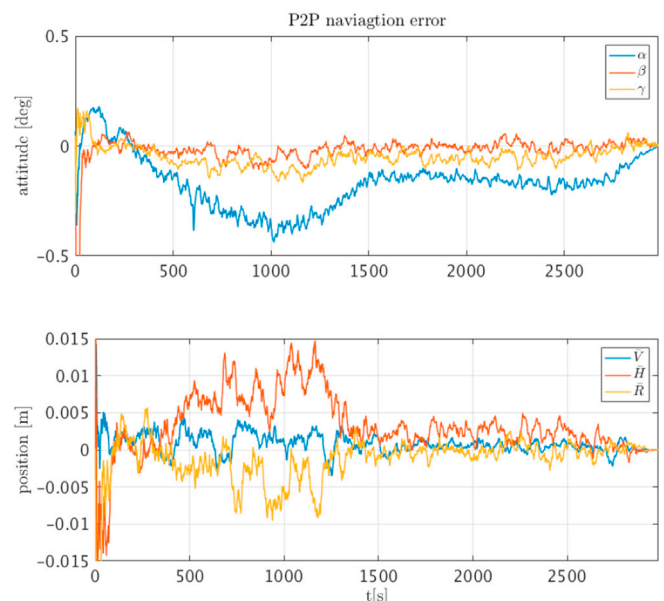

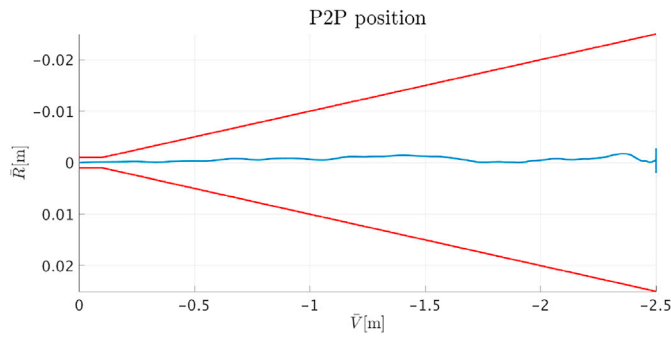**Fig. 28.** Navigation filter output using 5 central LEDs.

Fig. 29. Relative position in the docking port frame for the translation starting at 2.5 m. The red lines are the 1% of the range boundaries. (For interpretation of the references to colour in this figure legend, the reader is referred to the Web version of this article.)
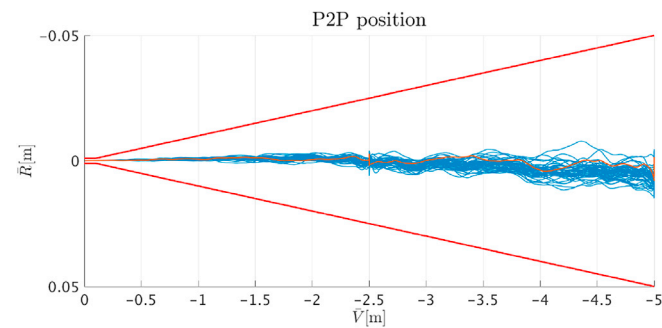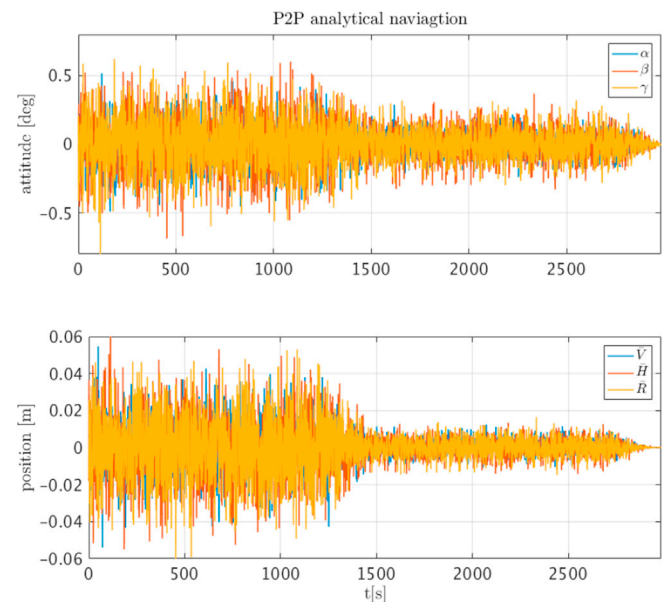

Fig. 30. Monte-Carlo simulation using 10% variation on the satellites masses and inertia tensors and 50% on the LEDs noise. The trajectory in orange shows the simulation with the nominal parameters. (For interpretation of the references to colour in this figure legend, the reader is referred to the Web version of this article.)

Fig. 31. Analytical solution using 5 central LEDs for the translation starting at 5 m until docking.

until 0.1 mm along each axis at docking. This solution could be used as primary navigation solution. However, if for some unforeseen reasons the LEDs could not be measured or only partially, this analytical solution would fail. The EKF remains thus preferred as it allows to propagate the navigation solution over few sample times, until the measurements are
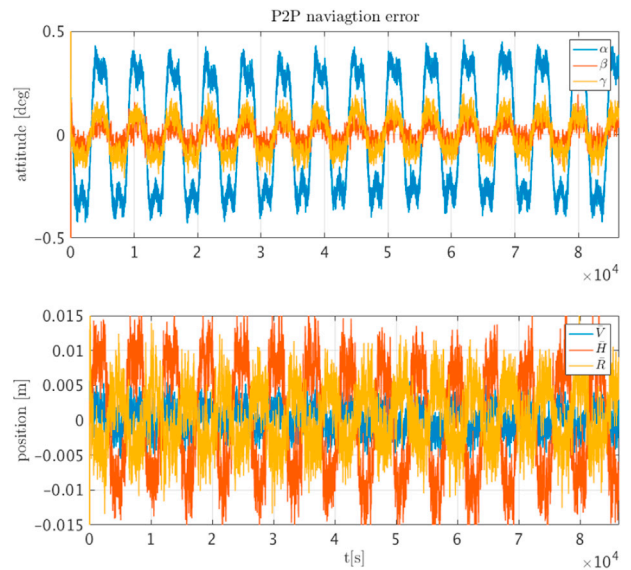

Fig. 32. 24 h station-keeping at 5 m range using the 5 LEDs EKF.

recovered and also provides a less noisy navigation solution which is desired from a control point of view. Finally, as already mentioned, the analytical solution will be used as a watchdog to monitor the performances of the EKF and as a contingency solution, adding an extra layer of robustness to the navigation function.

Fig. 32 shows the navigation error over 24 h of station-keeping at 5 m range from the docking port. The filter remains stable over time. As stated at the beginning of this section, the filter has converged in less than 5 min. The variations in the attitude and position are due to the residual dipoles inside the two Cubesats and the differential drag, which are the main source of external perturbations. The controller is not able to compensate for these exactly which is why periodic deviations can be observed in the navigation error.

5. Conclusion

Using a two sets of LEDs and a single COTS miniaturised camera, a novel and efficient measurement equation was derived for visual-based navigation supporting the final approach phase of cooperative CubeSat docking. The resulting equations can be solved analytically or used in an EKF. Such configuration allows the use of only one sensor all along the final approach trajectory. The drawback of the sought solution is that an out-of-plane LED is necessary. A small volume inside the CubeSat needs then to be dedicated to the pattern. However, this is considered to be acceptable from a satellite configuration perspective.

A reduced state space model was derived for the relative attitude and position between two arbitrary points on the target and chaser satellites. This dynamics used in the EKF, in combination with the LEDs measurements, allows to have an estimation of the relative position better than 1% of the range all over the approach trajectory (from 10 m until docking). The relative attitude determination at docking is always better than 0.2 deg and an actual pointing accuracy better than 2 deg is achievable. The LEDs detection is made robust to disturbances caused by the Sun or the Earth by actively tracking the LEDs using the EKF a posteriori estimated position. If this a posteriori position would not be available or for initialising the filter, an algorithm based on the geometrical features of the patterns can efficiently differentiate true LEDs from reflections. The performances of the geometrical features algorithm were tested and validated using an experimental set-up. It showed that the LEDs detection is not affected when the Sun is directly in the camera FoV, making the docking possible at any time and on a variety of orbits. Preliminary simulations shows that at docking, the relative attitude determination is

$\sim 10^{-3}$ deg around each axis and the relative position estimation is better than 0.1 mm along each axis. Furthermore, the proposed navigation solution is shown to be robust to mass and inertia tensor uncertainties of up to 10% and sensor noise uncertainties of up to 50%. Future work will include the simulation of the whole approach trajectory, including the fly-around, with realistic sensor and actuators noise error models and prediction of the closed-loop docking performance. The handover between the different navigation filters can then be better assessed and contingency modes will be discussed in case of LED failure. A stability analysis should be performed for the LQG as the EKF might remove the good frequency properties of the LQR. Although the 3 LEDs solution nominally requires the star trackers, simulations show that their loss leads to an attitude navigation solution only marginally violating the requirements. This should be further investigated with the complete GNC and errors in the loop as a standalone VBN solution could then be used in missions using only vision based techniques, removing the need for an ISL.

The level of accuracy obtained with the two filters that were presented in this paper gives confidence that an accurate navigation solution, tailored for CubeSat Rendezvous & Docking, can be obtained and that actual docking of CubeSats satisfying a lateral misalignment of 1.2 cm can be performed under any illumination conditions, simplifying the operations of such missions.

Acknowledgement

References

[1] W. Fehse, Automated Rendezvous and Docking of Spacecraft, vol. 16, Cambridge university press, 2005.

[2] B. Aldrin, Line-of-sight Guidance Techniques for Manned Orbital Rendezvous, Ph.D. thesis, Massachusetts Institute of Technology, 1963.

[3] S. D'Amico, J.-S. Ardaens, R. Larsson, Spaceborne autonomous formation-flying experiment on the PRISMA mission, J. Guid. Contr. Dynam. 35 (3) (2012) 834–850, https://doi.org/10.2514/1.55638.

[4] S. Leung, O. Montenbruck, Real-time navigation of formation-flying spacecraft using global-positioning-system measurements, J. Guid. Contr. Dynam. 28 (2) (2005) 226–235, https://doi.org/10.2514/1.7474.

[5] D. Pinard, S. Reynaud, P. Delpy, S.E. Strandmoe, Accurate and autonomous navigation for the ATV, Aero. Sci. Technol. 11 (6) (2007) 490–498, https://doi.org/10.1016/j.ast.2007.02.009.

[6] M. Ganet, I. Quinquis, J. Bourdon, P. Delpy, ATV GNC during rendezvous with ISS, in: DCSSS Conference, 2002.

[7] L. Kneip, D. Scaramuzza, R. Siegwart, A novel parametrization of the perspective-three-point problem for a direct computation of absolute camera position and orientation, CVPR 2011 (2011) 2969–2976, https://doi.org/10.1109/CVPR.2011.5995464.

[8] S.D.G.G. Bras, Deterministic Position and Attitude Estimation Methods, Ph.D. thesis, INSTITUTO SUPERIOR TECNICO, 2014.

[9] B.E. Tweddle, Computer Vision Based Navigation for Spacecraft Proximity Operations, Master thesis, 2010.

[10] V. A. Portsmouth, Vision Based Sensor and Navigation System for Autonomous Aerial Refueling.

[11] F. Sansone, A. Francesconi, L. Olivieri, F. Branz, Low-cost relative navigation sensors for miniature spacecraft and drones, in: Metrology for Aerospace (MetroAeroSpace), 2015 IEEE, IEEE, 2015, pp. 389–394.

[12] K.K. Gunnam, D.C. Hughes, J.L. Junkins, N. Kehtarnavaz, A vision-based DSP embedded navigation sensor, IEEE Sensor. J. 2 (5) (2002) 428–442.

[13] J.L. Junkins, D.C. Hughes, K.P. Wazni, V. Pariyapong, Vision-based navigation for rendezvous, docking and proximity operations, in: 22nd Annual AAS Guidance and Control Conference, Breckenridge, CO, 1999, pp. 99–9021.

[14] P. Bodin, R. Noteborn, R. Larsson, T. Karlsson, S. D'Amico, J.S. Ardaens, M. Delpech, J.-C. Berges, The prisma formation flying demonstrator: overview and conclusions from the nominal mission, Adv. Astronaut. Sci. 144 (2012) 441–460.

[15] M. Benn, Vision Based Navigation Sensors for Spacecraft Rendezvous and Docking, Ph.D. thesis, DTU Space, 2011.

[16] M. D'Errico (Ed.), Distributed Space Missions for Earth System Monitoring, Springer New York, New York, NY, 2013.

[17] M.A. Abidi, T. Chandra, Pose estimation for camera calibration and landmark tracking, in: IEEE International Conference on Robotics and Automation Proceedings vol. 1, 1990, pp. 420–426, https://doi.org/10.1109/ROBOT.1990.126013.

[18] P.C. Calhoun, R. Dabney, Solution to the Problem of Determining the Relative 6 DOF State for Spacecraft Automated Rendezvous and Docking, vol. 2466, 1995, pp. 175–184, https://doi.org/10.1117/12.211505.

[19] M.D. Shuster, S.D. Oh, Three-axis attitude determination from vector observations, J. Guid. Contr. Dynam. 4 (1) (1981) 70–77, https://doi.org/10.2514/3.19717.

[20] G. Casonato, G.B. Palmerini, Visual techniques applied to the ATV/1ss rendezvous monitoring, in: Aerospace Conference, 2004. Proceedings. 2004 IEEE, vol. 1, IEEE, 2004.

[21] C. Pirat, M. Richard-Noca, C. Paccolat, F. Belloni, R. Wiesendanger, D. Courtney, R. Walker, V. Gass, Mission design and GNC for in-orbit demonstration of active debris removal technologies with CubeSats, Acta Astronaut. 130 (2017) 114–127, https://doi.org/10.1016/j.actaastro.2016.08.038.

[22] Craig Underwood, Sergio Pellegrino, Vaios J. Lappas, Using Cubesat/Micro-Satellite Technology to Demonstrate the Autonomous Assembly of a Reconfigurable Space Telescope (AAREST), International Astronautical Congress (IAC), 2014.

[23] L. Olivieri, A. Francesconi, Design and test of a semiandrogynous docking mechanism for small satellites, Acta Astronaut. 122 (2016) 219–230, https://doi.org/10.1016/j.actaastro.2016.02.004.

[24] MIT Space Systems Lab, Design Document Universal Docking Port. URL http://ssl.mit.edu/spheres/spheresLibrary/documents/projectDocumentation/UDP_Design_Document_CDR.pdf Last checked 2017-03-17.

[25] Docking Systems. URL http://www.russianspaceweb.com/docking.html Last checked 2017-03-17.

[26] F. Ankersen, Guidance, Navigation, Control and Relative Dynamics for Spacecraft Proximity Maneuvers, Ph.D. thesis, Aalborg University, Aalborg, 2011.

[27] F.L. Markley, J.L. Crassidis, Fundamentals of Spacecraft Attitude Determination and Control, Springer New York, New York, NY, 2014.

[28] G.W. Hill, Researches in the lunar theory, Am. J. Math. 1 (1) (1878) 5–26.

[29] J.L. Crassidis, J.L. Junkins, Optimal Estimation of Dynamic Systems, CRC press, 2011.

[30] P.S. Maybeck, Stochastic Models, Estimation, and Control, vol. 2, Academic press, 1982.

[31] F.D. Busse, Precise Formation-state Estimation in Low Earth Orbit Using Carrier Differential GPS, 2003.

[32] Basler ace acA2500-14gm - Area Scan Camera. URL http://www.baslerweb.com/en/products/cameras/area-scan-cameras/ace/aca2500-14gm Last checked 2017-03-27.

[33] BP470 Blue Bandpass Filter, Jun. 2015. http://midopt.com/filters/bp470/. Last checked 2017-03-27.

[34] John C. Doyle, Guaranteed Margins for LQG Regulators.

[35] ST200. URL http://hyperiontechnologies.nl/products/st200-star-tracker/ Last checked 2017-06-23.